**Text S1. Adjustment of Lab-Reported ERs**

As noted in Sect. 2.4 of the main text, we adjust the emission ratios of acrolein and biacetyl downward by factors of 2.3 and 10, respectively, relative to the values reported by Koss et al. (2018). Here we provide some justification for these modifications.

For acrolein, instrument inter-comparisons during and after FIREX-AQ revealed a factor of 2.3 error in the quantification of the NOAA acrolein gas standard (personal communication, A. Wisthaler and M. Coggon, 2021). This is the same standard used in Koss et al. (2018).

For biacetyl (2,3-butanedione), it is likely that the work of Koss et al. (2018) did not account for all potential isomers in the PTR-ToF-MS interpretation. The molecular formula for this compound is $C_4H_6O_2$. Using GC-CIMS data, Koss et al. (2018) inferred contributions to this PTR-ToF-MS signal from biacetyl (87%), methacrylate (5%), and other unidentified compounds (8%). Previous work has suggested the presence of additional isomers that are not easily detected by GC. In one study of pine burning emissions, 2-oxobutanal emissions were 3 times greater than those of biacetyl (Schauer et al., 2001). 1,4-butanedial has also been observed in significant amounts in tobacco smoke (personal communication, A. Wisthaler, 2021). Based on the likely presence of these compounds, we conservatively reduce biacetyl by a factor of 10.

These adjustments reduce model over-prediction for APAN (produced solely from acrolein oxidation) and PAN (where biacetyl is a major precursor) in sensitivity simulations described in the main text.

**Text S2. Other oVOC**

Figure S12 shows the age progression of several other oVOC. Methanol is long-lived, and variability may reflect changing emissions or background conditions (Fig. S12a). A sharp rise in the methanol NEMR at 2 h may be another indicator of biogenic influence. Acetone and propanal are isomers ($C_3H_6O$) and are reported as a sum in the SEAC[4]RS dataset. Acetone is likely the dominant isomer given the short lifetime of propanal, and this is consistent with the small NEMR variability as the lifetime of acetone against oxidation is weeks (Fig. S12b). The hydroxyacetone NEMR is relatively constant with age, and model values agree with observations within uncertainties (Fig. S12c). The sum of MVK and MACR tells a story similar to acetaldehyde, with a biogenic signature at ~2 h and an over-rapid decline in the base simulation (Fig S12d). Results from other simulations are discussed in the main text when relevant.

**Text S3. Additional NO$_y$ Details**

Several studies have noted potential positive artifacts in $NO_2$ measurements due to decomposition of thermally unstable gases in the sample inlet or instrument (Browne et al., 2011; Silvern et al., 2018; Nault et al., 2015). This is unlikely to explain the discrepancy between observed and modeled $NO_x$ in simulations M0 and M1 (Fig. 2i) for several reasons. First, such an interference would need to affect both the TDLIF and chemiluminescence $NO_2$ measurements similarly, as these two measurements are strongly correlated: $NO_2(TDLIF) = 1.2*NO_2(CL) - 0.12$ ppbv, $r^2 = 1.00$. Second, if the artifact were due to known $NO_x$ reservoirs, the conversion efficiency would need to be substantial. The difference between observed and

modeled $NO_2$ in simulation M1 is $260 \pm 100$ pptv at ages beyond 5 h. Mean observed PAN and total PNs are 1.3 and 2.1 ppbv, respectively. Thus a conversion efficiency of 10% or more would be required to fully explain the model-measurement difference, and this is unlikely given typical aircraft cabin and inlet temperatures (< 40 °C). Modeled $HO_2NO_2$ and $CH_3O_2NO_2$ are < 5 pptv and < 1 pptv, respectively. We cannot rule out the potential influence of yet-unidentified $NO_x$ reservoirs, though previous work suggests such artifacts are likely limited to the upper troposphere (Silvern et al., 2018).

In addition to PAN (discussed in the main text), the SEAC[4]RS dataset includes observations of several other speciated peroxy nitrates (PNs) and a total PN measurement. Other speciated PNs, shown in Fig. S14, include peroxypropionyl nitrate (PPN), peroxyacryloyl nitrate (APAN), and peroxyisobutyryl nitrate (PiBN). In the base simulation, early PPN NEMR growth is under-predicted, but the model and observations converge after 2h. APAN and PiBN are generally under-predicted, due in part to a lack of VOC precursors in the base simulation. Changes in model PNs in simulation M1 reflect increases in VOC precursors. In particular, APAN is produced solely through oxidation of acrolein. All PNs increase upon addition of initial HONO or $pNO_3^-$ photolysis due to more $RO_2$ and $NO_2$. Conversely, heterogeneous $NO_2$ conversion to HONO has essentially no effect on PN NEMRs. In this case, decreasing $NO_2$ and increasing NO offsets the increase in $RO_2$.

Model-measurement comparison with the $\Sigma$PN observations tell a qualitatively similar story to the speciated data (Fig. S15a). This measurement (via thermal dissociation and laser-induced fluorescence detection of $NO_2$) is typically higher than the sum of speciated PN measurements (via thermal dissociation and detection of the peroxyacyl radicals), and in the first few hours this difference exceeds the combined uncertainty of the measurements. The reasons for this difference are unclear.

Alkyl nitrates (ANs) are minor products of the reaction of organic peroxy radicals ($RO_2$) with NO. The observed $\Sigma$AN NEMR is variable with no clear trend (Fig. S15b). The simulated $\Sigma$AN NEMR is relatively constant throughout each simulation, and all simulations fall within the variability of observed NEMRs.

**Text S4. Co-optimization of Unmeasured VOC and HONO**

Additional reactive VOC and HONO chemistry collectively improve model-measurement agreement for most species. HONO sensitivity simulations presented in Sect. 3.3 of the main text utilize the same initial VOC as simulation M1. Uncertainties in initial VOC concentrations stem from the age distribution and history of sampled smoke, adaptation of laboratory-derived emission factors to ambient conditions, potential errors in the emission factors themselves, and translation of unmeasured VOC to MCM species. Uncertainties in primary and secondary HONO are also significant, as we lack a HONO measurement for comparison and putative aerosol mechanisms are not well understood.

In an extended set of simulations, we simultaneously tune initial unmeasured VOC, initial HONO, and $pNO_3^-$ photolysis. For these runs, default values for initial unmeasured VOC concentrations (M1), initial HONO (M2c), and particulate nitrate photolysis rate (M3b) are each independently scaled by factors of 0, 0.25, 0.5, 0.75, and 1. Iterating over all combinations yield 125 simulations. Results from these simulations are analyzed in terms of normalized mean bias (NMB) (Gustafson and Yu, 2012) relative to observed NEMR age profiles. Heterogeneous $NO_2$ uptake is not included, as tests with this mechanism indicate that it degrades agreement with observed ozone and other species.

Figure S26a-e shows the NMB of the ozone NEMR for each of the 125 simulations. Consistent with the examples presented in the main text, this bias trends negative with increasing VOC and positive with increasing initial or secondary HONO. Multiple scaling combinations produce a net $O_3$ NEMR NMB near zero (Fig. S27a). In general, increasing initial unmeasured VOC concentrations necessitates higher HONO to maintain agreement with observed $O_3$. Initial and secondary HONO similarly influence the overall $O_3$ NEMR NMB, though this simplified metric masks age-dependent differences (Fig. S28).

Figures S26f-o and S27b-c show analogous NMB gradients and minimum-value isopleths for $NO_x$ and PAN NEMRs. Compared to the results for ozone, higher HONO is required to close the $NO_x$ budget for any given value of unmeasured VOC. PAN bias can be minimized at higher VOC, but only with low initial HONO and relatively slow $pNO_3^-$ photolysis. No combination of scaling factors optimizes agreement among all observations.

# References

Akagi, S. K., Yokelson, R. J., Wiedinmyer, C., Alvarado, M. J., Reid, J. S., Karl, T., Crounse, J. D., and Wennberg, P. O.: Emission factors for open and domestic biomass burning for use in atmospheric models, Atmospheric Chem. Phys., 11, 4039–4072, https://doi.org/10.5194/acp-11-4039-2011, 2011.

Browne, E. C., Perring, A. E., Wooldridge, P. J., Apel, E., Hall, S. R., Huey, L. G., Mao, J., Spencer, K. M., Clair, J. M. S., Weinheimer, A. J., Wisthaler, A., and Cohen, R. C.: Global and regional effects of the photochemistry of $CH_3O_2NO_2$: evidence from ARCTAS, Atmospheric Chem. Phys., 11, 4209–4219, https://doi.org/10.5194/acp-11-4209-2011, 2011.

Gustafson, W. and Yu, S.: Generalized approach for using unbiased symmetric metrics with negative values: normalized mean bias factor and normalized mean absolute error factor, Atmospheric Sci. Lett., 13, 262–267, https://doi.org/10.1002/asl.393, 2012.

Koss, A. R., Sekimoto, K., Gilman, J. B., Selimovic, V., Coggon, M. M., Zarzana, K. J., Yuan, B., Lerner, B. M., Brown, S. S., Jimenez, J. L., Krechmer, J., Roberts, J. M., Warneke, C., Yokelson, R. J., and de Gouw, J.: Non-methane organic gas emissions from biomass burning: identification, quantification, and emission factors from PTR-ToF during the FIREX 2016 laboratory experiment, Atmospheric Chem. Phys., 18, 3299–3319, https://doi.org/10.5194/acp-18-3299-2018, 2018.

Nault, B. A., Garland, C., Pusede, S. E., Wooldridge, P. J., Ullmann, K., Hall, S. R., and Cohen, R. C.: Measurements of CH3O2NO2 in the upper troposphere, Atmospheric Meas. Tech., 2, 987–997, https://doi.org/10.5194/amt-8-987-2015, 2015.

Peng, Q., Palm, B. B., Melander, K. E., Lee, B. H., Hall, S. R., Ullmann, K., Campos, T., Weinheimer, A. J., Apel, E. C., Hornbrook, R. S., Hills, A. J., Montzka, D. D., Flocke, F., Hu, L., Permar, W., Wielgasz, C., Lindaas, J., Pollack, I. B., Fischer, E. V., Bertram, T. H., and Thornton, J. A.: HONO Emissions from Western U.S. Wildfires Provide Dominant Radical Source in Fresh Wildfire Smoke, Environ. Sci. Technol., 54, 5954–5963, https://doi.org/10.1021/acs.est.0c00126, 2020.

Schauer, J. J., Kleeman, M. J., Cass, G. R., and Simoneit, B. R. T.: Measurement of Emissions from Air Pollution Sources. 3. C1−C29 Organic Compounds from Fireplace Combustion of Wood, Environ. Sci. Technol., 35, 1716–1728, https://doi.org/10.1021/es001331e, 2001.

Silvern, R. F., Jacob, D. J., Travis, K. R., Sherwen, T., Evans, M. J., Cohen, R. C., Laughner, J. L., Hall, S. R., Ullmann, K., Crounse, J. D., Wennberg, P. O., Peischl, J., and Pollack, I. B.: Observed NO/NO2 Ratios in the Upper Troposphere Imply Errors in NO-NO2-O3 Cycling Kinetics or an Unaccounted NOx Reservoir, Geophys. Res. Lett., 45, 4466–4474, https://doi.org/10.1029/2018GL077728, 2018.

Theys, N., Volkamer, R., Müller, J.-F., Zarzana, K. J., Kille, N., Clarisse, L., De Smedt, I., Lerot, C., Finkenzeller, H., Hendrick, F., Koenig, T. K., Lee, C. F., Knote, C., Yu, H., and Van Roozendael, M.: Global nitrous acid emissions and levels of regional oxidants enhanced by wildfires, Nat. Geosci., 13, 681–686, https://doi.org/10.1038/s41561-020-0637-7, 2020.

Toon, O. B., Maring, H., Dibb, J., Ferrare, R., Jacob, D. J., Jensen, E. J., Luo, Z. J., Mace, G. G., Pan, L. L., Pfister, L., Rosenlof, K. H., Redemann, J., Reid, J. S., Singh, H. B., Thompson, A. M., Yokelson, R., Minnis, P., Chen, G., Jucks, K. W., and Pszenny, A.: Planning, implementation, and scientific goals of the Studies of Emissions and Atmospheric Composition, Clouds and Climate Coupling by Regional Surveys (SEAC(4)RS) field mission, J. Geophys. Res.-ATMOSPHERES, 121, 4967–5009, https://doi.org/10.1002/2015JD024297, 2016.

Table S1. SEAC[4]RS measurement details.

| Measurement | Instrument[a] | Accuracy |
|---|---|---|
| Pressure | MMS | < 1% |
| Temperature | | |
| $H_2O$ | DLH | 5% |
| CO | DACOM | 2% |
| Photolysis frequencies | CAFS | 12 – 20%[b] |
| $O_3$ | NOyO3 | 3% |
| NO | | 4% |
| $NO_2$ | | 7% |
| $NO_2$ | TDLIF | 5% |
| $\Sigma PN$ | | 10% |
| $\Sigma AN$ | | 15% |
| $H_2O_2$ | CIT-CIMS | 30% |
| $HNO_3$ | | 30% |
| HCN | | 50% |
| Peroxyacetic acid | | 50% |
| Hydroxyacetone | | 40% |
| Hydroxymethyl hydroperoxide | | 50% |
| Ethene hydroxynitrate | | 50% |
| Propene hydroxynitrate | | 30% |
| Butene hydroxynitrate | | 50% |
| Ethanal nitrate | | 50% |
| Propanone nitrate | | 50% |
| Isoprene hydroxynitrate | | 30% |
| PAN | GT-CIMS | 15% |
| PPN | | 20% |
| APAN | | 40% |
| PiBN | | 40% |
| VOC[c] | WAS | 5% |
| Acetonitrile | PTR-MS | 15% |
| Methanol | | 15% |
| Acetaldehyde | | 15% |
| Acetone + propanal | | 5% |
| MVK + MACR | | 10% |
| Isoprene + Furan | | 5% |
| HCHO | ISAF | 10% |
| | CAMS | 4% |
| Particulate nitrate | AMS | 17% |
| Aerosol surface area | LAS | 20% |
| Solar irradiance | BBR | 5% |

[a]See Toon et al. (2016) for details.
[b]Varies based on uncertainties in recommended cross sections and quantum yields.
[c]Methyl nitrate, ethyl nitrate, isopropyl nitrate, n-propyl nitrate, 2-butyl nitrate, 3-methyl-2-butyl nitrate, 3-pentyl nitrate, 2-pentyl nitrate, methane, ethane, propane, n-butane, isobutene, n-pentane, isopentane, n-hexane, 2-methyl pentane, 3-methyl pentane, 2,3-dimethylbutane, n-heptane, ethene,

propene, 1-butene, cis-2-butene, trans-2-butene, isobutene, 1,3-butadiene, 1-pentene, propadiene, benzene, toluene, ethyl benzene, o-xylene, m-xylene + p xylene (measured as sum, assumed 50%/50% distribution), isoprene, $\alpha$-pinene, $\beta$-pinene.

Table S2. MCM assignments for unmeasured VOC.

| Koss ID | Koss Formula | MCM Name | Emission Ratio ($\Delta X/\Delta CO$) |
|---|---|---|---|
| **Species with direct MCM analogues** | | | |
| Acetic acid + glycolaldehyde | C2H4O2H | CH3CO2H | 10.7633 |
| Acetic acid + glycolaldehyde | C2H4O2H | HOCH2CHO | 5.3013 |
| HONO | HNO2H | HONO | 3.2765 |
| 2-furfural + 3-furfural + other HCO2 | C5H4O2H | FURFURAL2 | 3.2625 |
| Formic acid | CH2O2H | HCOOH | 2.3024 |
| 2-(3H)Furanone | C4H4O2H | BZFUONE | 1.8951 |
| 5-Methyl furfural +Benzene diols (=catechol, resorcinol) | C6H6O2H | MFURFURAL | 1.8749 |
| 5-Methyl furfural +Benzene diols (=catechol, resorcinol) | C6H6O2H | CATECHOL | 1.8749 |
| Guaiacol (=2-methoxyphenol) | C7H8O2H | GUAIACOL | 1.8696 |
| Acrolein | C3H4OH | ACR | 1.8446 |
| 2-Methylphenol (=o-cresol) + anisol | C7H8OH | CRESOL | 1.7222 |
| Phenol | C6H6OH | PHENOL | 1.7124 |
| 2-Methoxy-4-methylphenol (= creosol) | C8H10O2H | MGUAIACOL | 1.1605 |
| 2-methylfuran + 3-methylfuran + general HCO | C5H6OH | M2F | 0.9074 |
| methyl acetate + ethyl formate + hydroxyacetone | C3H6O2H | METHACET | 0.9060 |
| Pyruvaldehyde (=methyl glyoxal) + acrylic acid | C3H4O2H | MGLYOX | 0.7083 |
| Pyruvaldehyde (=methyl glyoxal) + acrylic acid | C3H4O2H | ACO2H | 0.7083 |
| Glyoxal | C2H2O2H | GLYOX | 0.7048 |
| MEK + butanal + 2-methylpropanal | C4H8OH | MEK | 0.5282 |
| MVK + methacrolein + crotonaldehyde | C4H6OH | C4ALDB | 0.5053 |
| Quinone (=p-Benzoquinone) | C6H4O2H | PBZQONE | 0.4795 |
| Ethanol | C2H6OH | C2H5OH | 0.4481 |
| 2,5-dimethyl furan + 2-ethylfuran + other C2 substituted furans | C6H8OH | DIM25FURAN | 0.4226 |
| C2 Phenols + methyl anisol | C8H10OH | OXYLOL | 0.4222 |
| methyl acetate + ethyl formate + hydroxyacetone | C3H6O2H | ETHFORM | 0.3624 |
| Acetic anhydride | C4H6O3H | METHCOACET | 0.3198 |
| Benzaldehyde | C7H6OH | BENZAL | 0.1962 |
| 2-methylfuran + 3-methylfuran + general HCO | C5H6OH | M3F | 0.1779 |
| 2,3-butanedione + methyl acrylate + other HCO2 | C4H6O2H | BIACET | 0.1650 |
| Styrene | C8H8H | STYRENE | 0.1625 |
| 2-furfural + 3-furfural + other HCO2 | C5H4O2H | FURFURAL3 | 0.1554 |
| syringol | C8H10O3H | SYRINGOL | 0.1485 |
| Tolualdehyde | C8H8OH | PXYLAL | 0.0900 |
| Tolualdehyde | C8H8OH | MXYLAL | 0.0900 |
| 3-methyl-2-butanone + 2-methylbutanal+3-methylbutanal+2-pentanone +3-pentanone | C5H10OH | MIPK | 0.0877 |

| | | | |
|---|---|---|---|
| MEK + butanal + 2-methylpropanal | C4H8OH | IPRCHO | 0.0870 |
| Tolualdehyde | C8H8OH | OXYLAL | 0.0772 |
| 3-methyl-2-butanone + 2-methylbutanal+3-methylbutanal+2-pentanone +3-pentanone | C5H10OH | MPRK | 0.0653 |
| Methyl benzoic acid | C8H8O2H | PXYLCO2H | 0.0652 |
| Methyl benzoic acid | C8H8O2H | MXYLCO2H | 0.0652 |
| Sesquiterpenes | C15H24H | BCARY | 0.0651 |
| Methyl benzoic acid | C8H8O2H | OXYLCO2H | 0.0559 |
| 3-methyl-2-butanone + 2-methylbutanal+3-methylbutanal+2-pentanone +3-pentanone | C5H10OH | DIEK | 0.0428 |
| Pyruvic acid | C3H4O3H | CH3COCO2H | 0.0407 |
| heptanal + 2,4-dimethyl-3-pentanone + heptanone | C7H14OH | C6H13CHO | 0.0317 |
| heptanal + 2,4-dimethyl-3-pentanone + heptanone | C7H14OH | HEPT3ONE | 0.0186 |
| Dimethyl sulfide | C2H6SH | DMS | 0.0116 |
| hexanal + hexanones | C6H12OH | C5H11CHO | 0.0110 |
| hexanal + hexanones | C6H12OH | HEX2ONE | 0.0070 |
| MEK + butanal + 2-methylpropanal | C4H8OH | C3H7CHO | 0.0062 |
| hexanal + hexanones | C6H12OH | HEX3ONE | 0.0054 |
| 3-methyl-2-butanone + 2-methylbutanal+3-methylbutanal+2-pentanone +3-pentanone | C5H10OH | BUT2CHO | 0.0041 |
| 3-methyl-2-butanone + 2-methylbutanal+3-methylbutanal+2-pentanone +3-pentanone | C5H10OH | C3ME3CHO | 0.0041 |

| **Species mapped to MCM using OH reaction rate coefficient and molecular formula** | | | |
|---|---|---|---|
| 2-furanmethanol + other HCO2 | C5H6O2H | MEKAOH | 1.7325 |
| 5-(hydroxymethyl)-2-furfural | C6H6O3H | C512OOH | 1.0774 |
| 5-hydroxymethyl-2[3H]-furanone | C5H6O3H | C512OOH | 0.9055 |
| 2-hydroxy-3-methyl-2-cyclopenten-1-one | C6H8O2H | HEX3ONDOOH | 0.7753 |
| Product of levoglucosan dehydration (pyrolysis) | C6H8O4H | M3HEXANO3 | 0.6436 |
| 2,5-di(hydroxymethyl)furan + Methyl hydroxy dihydrofurfural | C6H8O3H | CO1M22CHO | 0.5730 |
| Methyl methacrylate + other HCO2 | C5H8O2H | HO2CO4CHO | 0.5689 |
| 3-methyl-3-butene-2-one + cyclopentanone + HCO1 isomers | C5H8OH | PEBOH | 0.5685 |
| 5-Hydroxy 2-furfural/2-furoic acid | C5H4O3H | C4DBDIKET | 0.4838 |
| 2,4-Cyclopentadiene-1-one + 2 other HCO isomers | C5H4OH | HO25C6 | 0.4779 |
| Vanillin | C8H8O3H | C7CO4EDB | 0.4712 |
| Methyl propanoate | C4H8O2H | MAE | 0.4602 |
| Vinyl guaiacol | C9H10O2H | LIMKET | 0.3705 |
| Acetamide | C2H5NOH | ACO2H | 0.3637 |
| 5-hydroxymethyl tetrahydro 2-furanone + 5-hydroxy tetrahydro 2-furfural | C5H8O3H | CO2M33CO3H | 0.3543 |
| C3 furan + various HCO | C7H10OH | HO25C7 | 0.3052 |
| 1-Buten-3-yne | C4H4H | ACR | 0.2894 |
| pyrrole + butene nitrile isomers | C4H5NH | C5H8 | 0.2417 |

| | | | |
|---|---|---|---|
| Eugenol + isoeugenol | C10H12O2H | LIMKET | 0.2415 |
| Nitromethane | CH3NO2H | | 0.2264 |
| 2-propynal | C3H2OH | ACR | 0.2091 |
| Dihydro furandione | C4H4O3H | HMACO3H | 0.2083 |
| Hydroxy benzoquinone | C6H4O3H | M3HEXANO3 | 0.2058 |
| 2-hydroxybenzaldehyde (=Salicylaldehyde) | C7H6O2H | HO3C5CHO | 0.1526 |
| Pyridine + pentadienenitriles | C5H5NH | M23C4 | 0.1432 |
| Naphthalene | C10H8H | UDECOH | 0.1388 |
| C9 Aromatics | C9H12H | DECOH | 0.1255 |
| methane thiol | CH4SH | CHCL2CHO | 0.1243 |
| Methyl benzofuran | C9H8OH | NOPINAOH | 0.1191 |
| C6 Diones + C6 1-DBE esters | C6H10O2H | IEB4CHO | 0.1141 |
| Acrylonitrile | C3H3NH | DICLETOH | 0.1138 |
| Methyl thiophenes | C5H6SH | ETBE | 0.1098 |
| 1,3-Cyclopentadiene | C5H6H | ME2BUT2ENE | 0.1055 |
| dimethylbenzofuran | C10H10OH | NOPINAOH | 0.1045 |
| Methyl cyclopentanone + cyclohexanone + other ketones | C6H10OH | M3PECOOH | 0.0927 |
| methyl isocyanate + hydroxyacetonitrile | C2H3NOH | ETHOX | 0.0871 |
| 3-methylacetophenone | C9H10OH | C8BCCO | 0.0870 |
| Methyl propenyl benzene + ethyl styrene | C10H12H | C7MOCOCO3H | 0.0860 |
| Formamide | CH3NOH | CCL3CHO | 0.0842 |
| Indane + methyl styrenes + propenyl benzenes | C9H10H | APINENE | 0.0820 |
| Benzofuran | C8H6OH | NOPINAOH | 0.0819 |
| Propane nitrile | C3H5NH | CH3CCL2OH | 0.0797 |
| C10 Aromatics | C10H14H | NC9H20 | 0.0792 |
| Methyl pyrrole isomers + Pentene nitrile isomers | C5H7NH | ME2BUT1ENE | 0.0743 |
| C6 esters | C6H12O2H | EMPHCOME | 0.0690 |
| Benzonitrile | C7H5NH | MC6OTKETOH | 0.0685 |
| Thiophene | C4H4SH | IBUTOL | 0.0610 |
| 2-methyl pyridine + 3-methylpyridine | C6H7NH | MIPK | 0.0603 |
| Dihydronaphthalene | C10H10H | C108NO3 | 0.0574 |
| Dihydropyrrole + butane nitrile | C4H7NH | CL12PRCHO | 0.0570 |
| Methyl naphthalene | C11H10H | C129CO | 0.0552 |
| Propiolic acid | C3H2O2H | ALLYLOH | 0.0542 |
| Methyl chavicol (estragole) | C10H12OH | PINAL | 0.0522 |
| Ethylcyclopentanone | C7H12OH | HM33C4OH | 0.0497 |
| 1,3-dimethylnaphthalene | C12H12H | NC1313OH | 0.0493 |
| Indene + propynyl benzene isomer | C9H8H | BPINENE | 0.0488 |
| 4-pyridinol | C5H5NOH | TBUACET | 0.0427 |
| Camphor + other oxygenated monoterpenes | C10H16OH | C828PAN | 0.0396 |
| 2-ethenyl benzofuran | C10H8OH | NOPINAOH | 0.0379 |

| | | | |
|---|---|---|---|
| 2,5-dimethyl pyrrole + 1-ethylpyrrole + other C2 substituted pyrroles | C6H9NH | CYHXONAOOH | 0.0366 |
| Ethenamine | C2H5NH | C2H6 | 0.0346 |
| Nitrobenzene | C6H5NO2H | ACECOCOCH3 | 0.0325 |
| Pentanenitriles | C5H9NH | C5PAN6 | 0.0314 |
| Phenylacetylene | C8H6H | MC6OTKETOH | 0.0276 |
| nitrotoluene | C7H7NO2H | ACCOPRONE | 0.0246 |
| dihydroxy pyridine + methyl maleimide | C5H5NO2H | M3PEAOH | 0.0225 |
| pyridine aldehyde + methylfuronitrile + nitrosobenzene | C6H5NOH | H25M2C6 | 0.0211 |
| benzeneacetonitrile | C8H7NH | NC71CO | 0.0207 |
| C11 aromatics | C11H16H | C129CO | 0.0197 |
| ethylindene | C11H12H | BPINENE | 0.0194 |
| 2-furancarbonitrile + 3-furancarbonitrile | C5H3NOH | H2M3C4CHO | 0.0189 |
| Trimethylamine | C3H9NH | MEPROPENE | 0.0181 |
| dimethyl pyridine + ethylpyridine + heptylnitriles | C7H9NH | M2PEDOH | 0.0172 |
| C7 acrylonitrile | C7H11NH | C6CO2OHPAN | 0.0169 |
| Acenaphthylene | C12H8H | DDEC3ONE | 0.0164 |
| Propene amine | C3H7NH | PXYL | 0.0158 |
| Cineole + other oxygenated monoterpenes | C10H18OH | HO36C10 | 0.0137 |
| C12 aromatics | C12H18H | C126CHO | 0.0113 |
| 4-methylpentanenitrile | C6H11NH | MPRK | 0.0109 |
| Carbon suboxide | C3O2H | EOX2COMEOH | 0.0104 |
| Methyl benzeneacetonitrile | C9H9NH | C920PAN | 0.0104 |
| Dimethyl disulfide | C2H6S2H | PXYCATECH | 0.0098 |
| C13 aromatics | C13H20H | BCKET | 0.0097 |
| butene nitrates | C4H7NO3H | NPRACBOOH | 0.0078 |
| Vinylpyridine | C7H7NH | THEX2ENE | 0.0066 |
| decanal | C10H20OH | NC11H24 | 0.0065 |
| Nitrofuran | C4H3NO3H | MALDALCO3H | 0.0064 |
| Methanimine | CH3NH | C2H6 | 0.0062 |
| Propiolonitrile (=propyne nitrile) | C3HNH | DICLETOH | 0.0058 |
| Butene amine | C4H9NH | MVK | 0.0055 |
| nitroethene | C2H3NO2H | PROPACID | 0.0054 |
| Ethylnylpyrrole | C6H6N | CYHXONAOOH | 0.0046 |
| methane diol | CH4O2H | ETHOXOOH | 0.0041 |
| Nitroethane or ethane nitrite | C2H5NO2H | ETHOX | 0.0035 |
| Ethylamine + dimethylamine | C2H7NH | CRESOL | 0.0030 |
| Dihydro pyridine | C8H9NH | C5PAN6 | 0.0029 |
| Nitropropanes | C3H7NO2H | PROPACID | 0.0018 |
| Cyanoallene isomers | C4H3NH | IPECOH | 0.0013 |
| C8 nitriles | C8H15NH | HEPT3ONE | 0.0012 |
| Dimethyl trisulfide | C2H6S3H | PXYCATECH | 0.0011 |
| n-sulfinyl methanamine | CH3NOSH | C2H6 | 0.0003 |
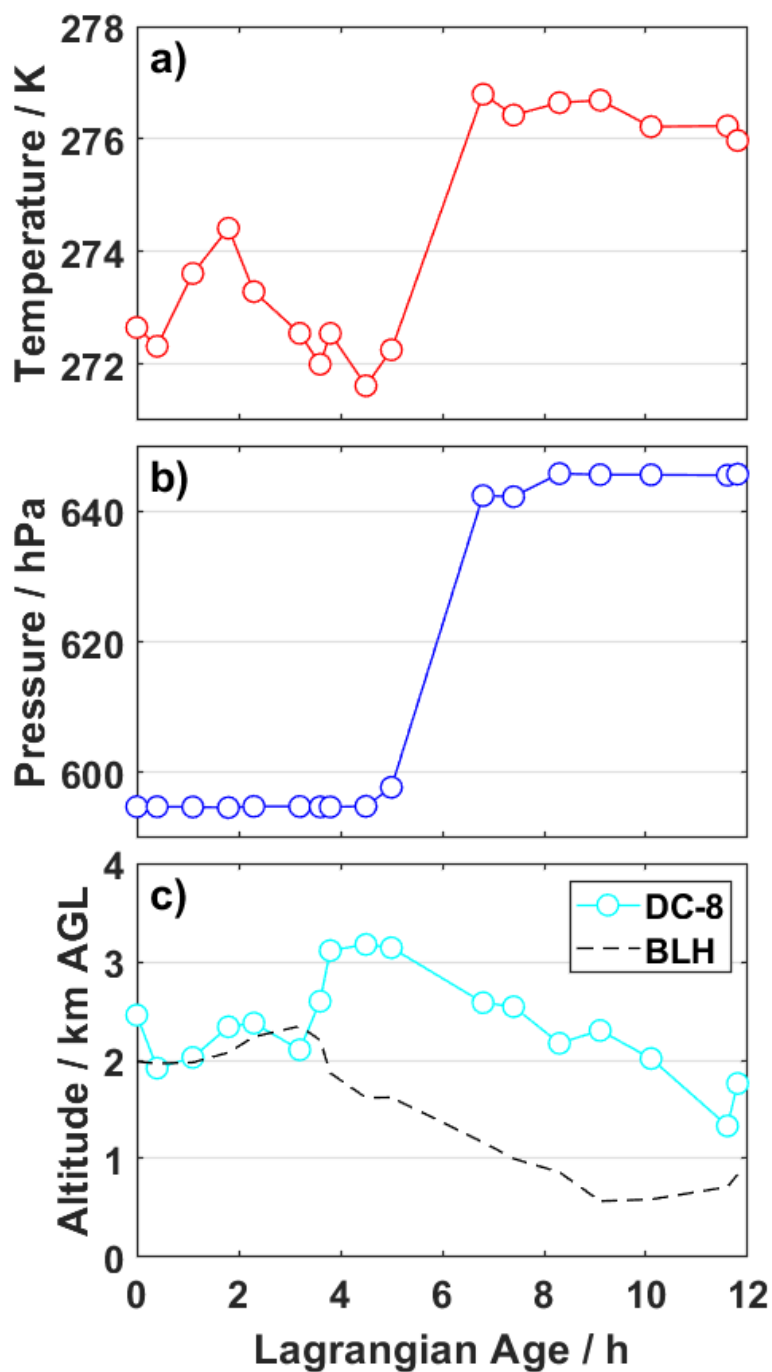
Figure S1. DC-8 sampling temperature (a), atmospheric pressure (b), and altitude above ground level (c, cyan circles) as a function of plume Lagrangian Age. The dashed line in (c) denotes the boundary layer height relative to ground level based on output from the two meteorological datasets used for trajectory analysis.
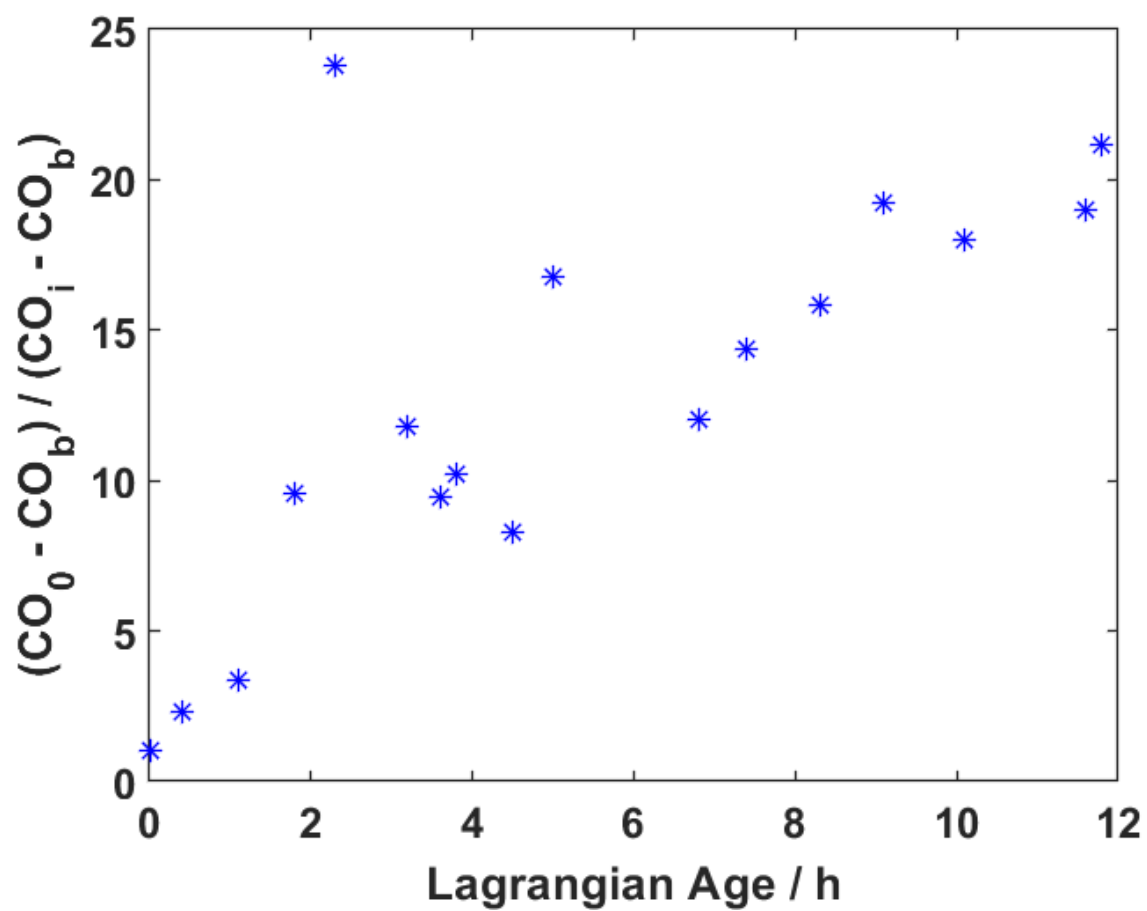
Figure S2. Dilution factor for each WAS plume sample, calculated as the ratio of initial to sample-time background-corrected CO.
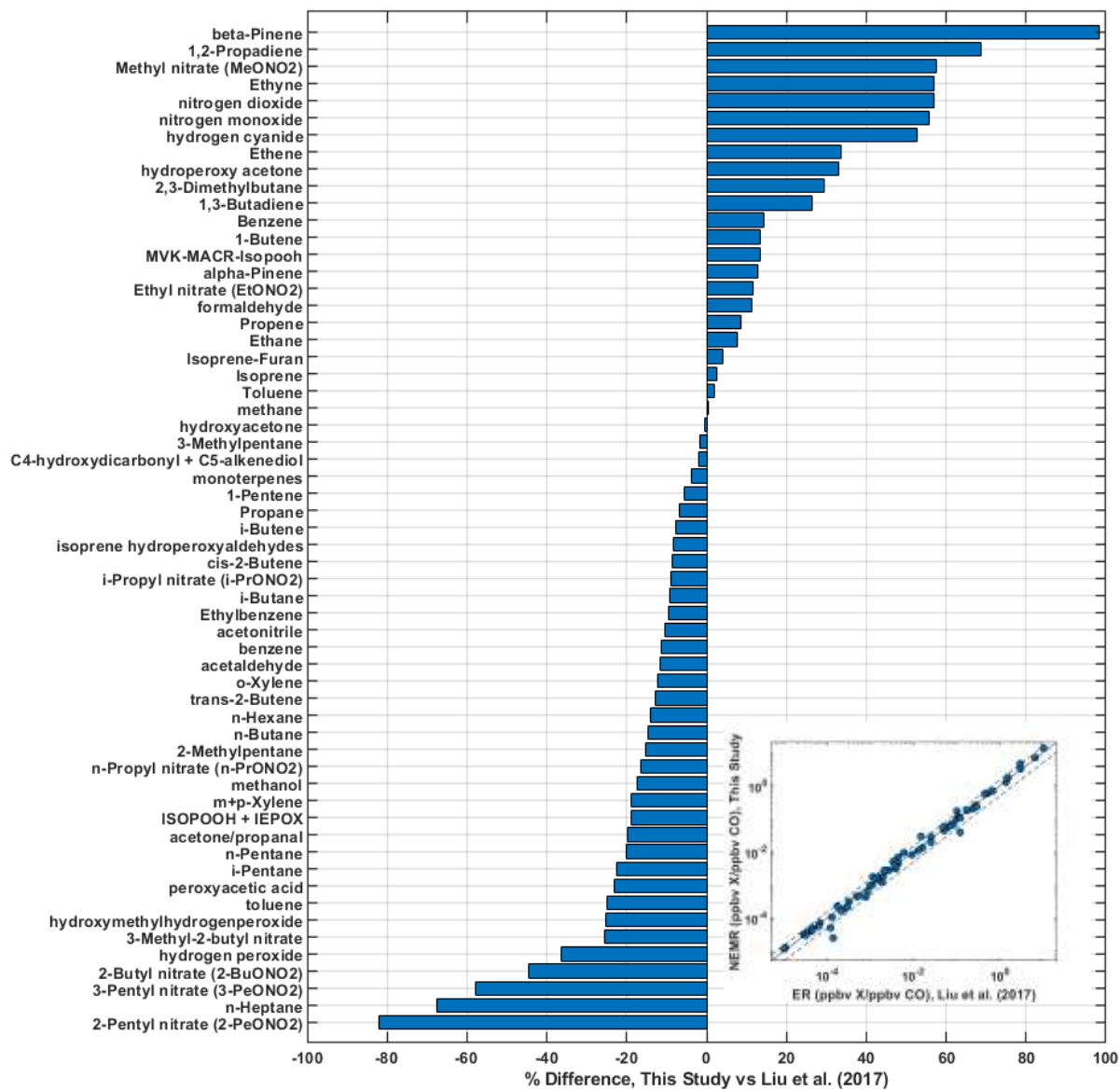
Figure S3. Comparison of normalized excess mixing ratios (NEMR) from the "source" sample of this study and the Rim Fire emission ratios (ERs) reported by Liu et al. (2017). Both NEMR and ER values are normalized to excess CO. In the species-specific plot, positive values correspond to species with a higher ratio in long-axis source sample, and values with ER < $10^{-4}$ ppbv / ppbv are excluded. In the inset, the solid line is the 1:1 relationship and dashed lines are ±50%.
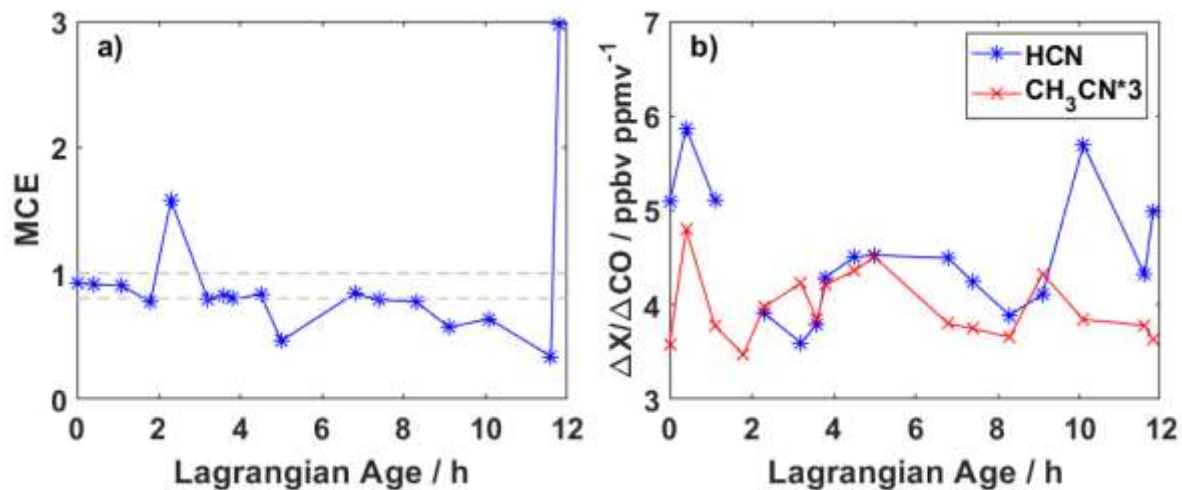
Figure S4. Modified combustion efficiency (MCE) (a) and NEMRs for formonitrile and acetonitrile (b). MCE is defined as $\Delta CO_2 / (\Delta CO + \Delta CO_2)$. Gray dashed lines in (a) denote the range of $0.8 - 1$ typical of wildfires (Akagi et al., 2011).
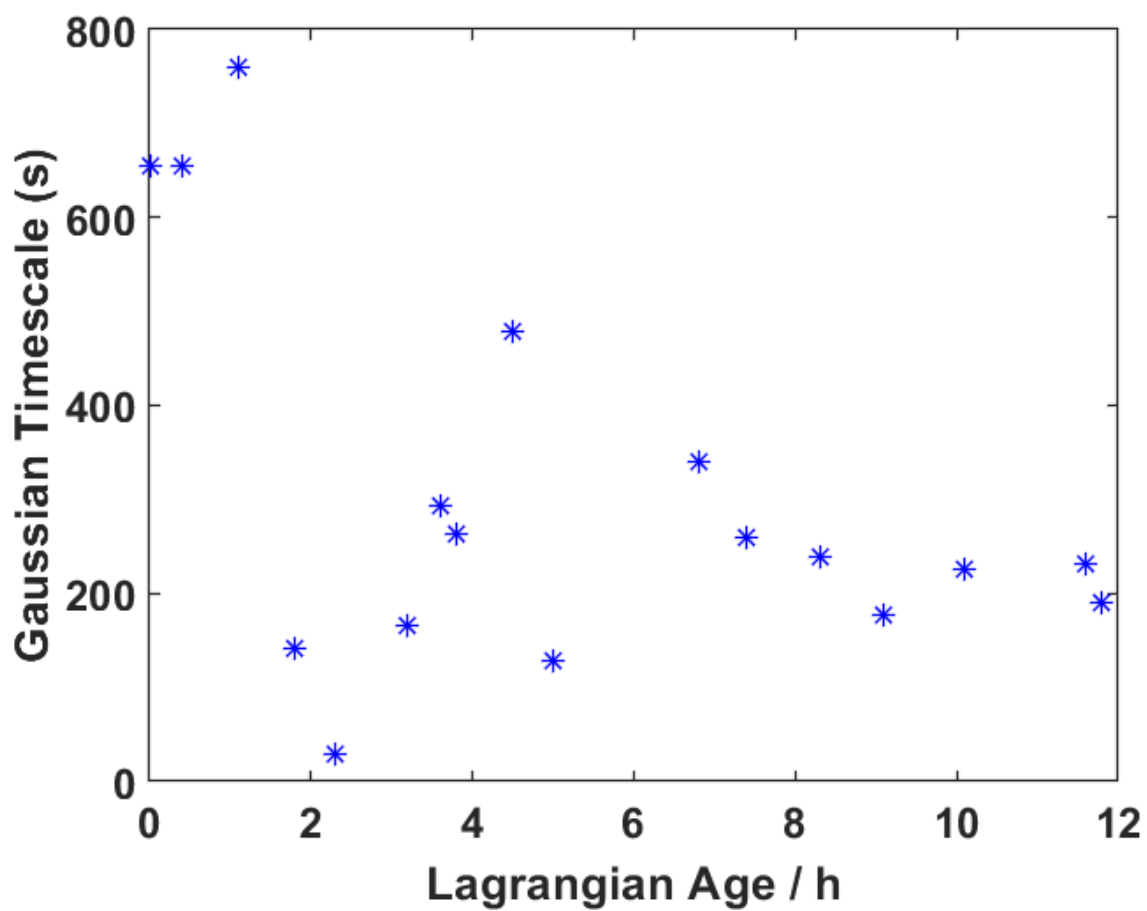
Figure S5. Gaussian dilution timescale for each model puff, calculated from observations of the decay of CO and Eqn. (2) as described in the main text.
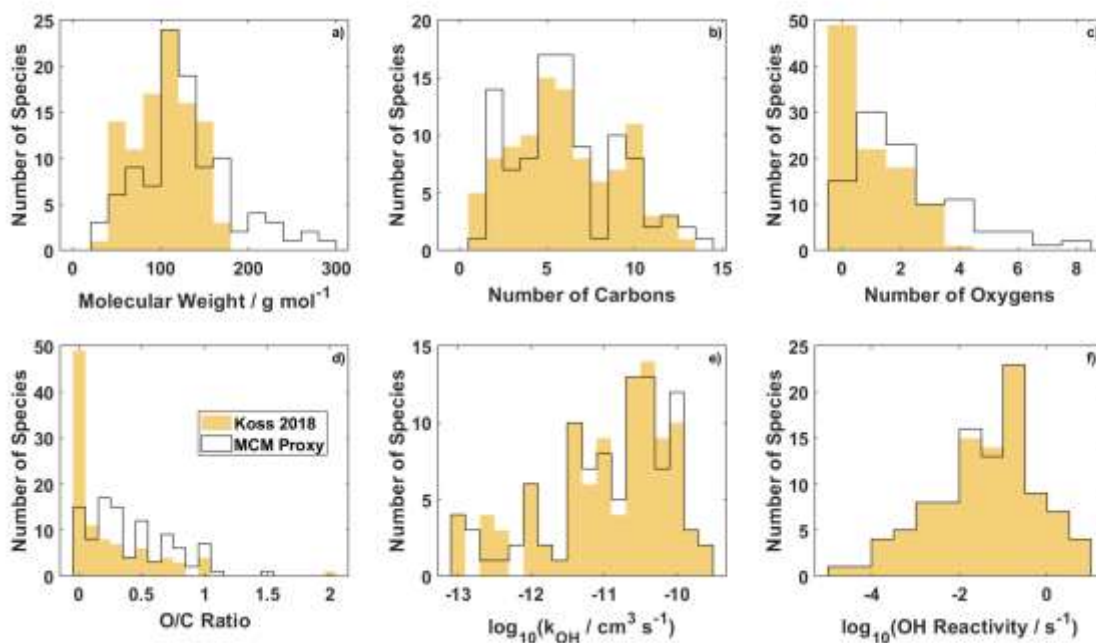
Figure S6. Comparison of chemical metrics for non-MCM unmeasured VOC from Koss et al. (2018) and MCM proxies (see Sect. 2.4.1 and Table S2). (a) Molecular weight, (b) number of carbons per molecule, (c) number of oxygens per molecule, (d) oxygen/carbon ratio per molecule, (e) OH reaction rate coefficient, and (f) initial OH reactivity. Note that (e) and (f) are on a log scale.
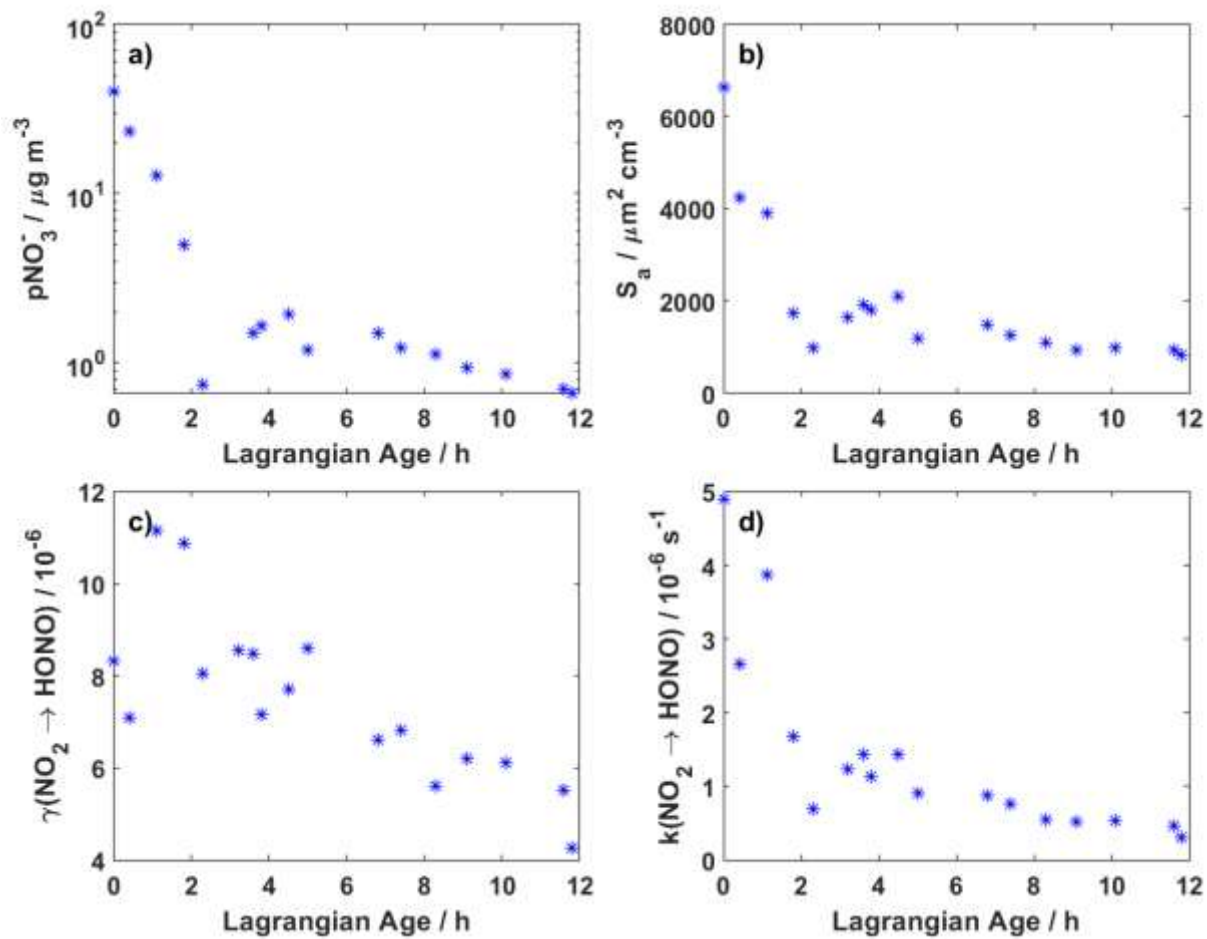
Figure S7. Observed and derived aerosol-related properties as a function of plume age: AMS-observed particulate nitrate mass concentration (a), LAS-observed aerosol surface area (b), calculated reactive uptake coefficient for $NO_2$ conversion to HONO (c), and calculated first order rate coefficient for the same (d).
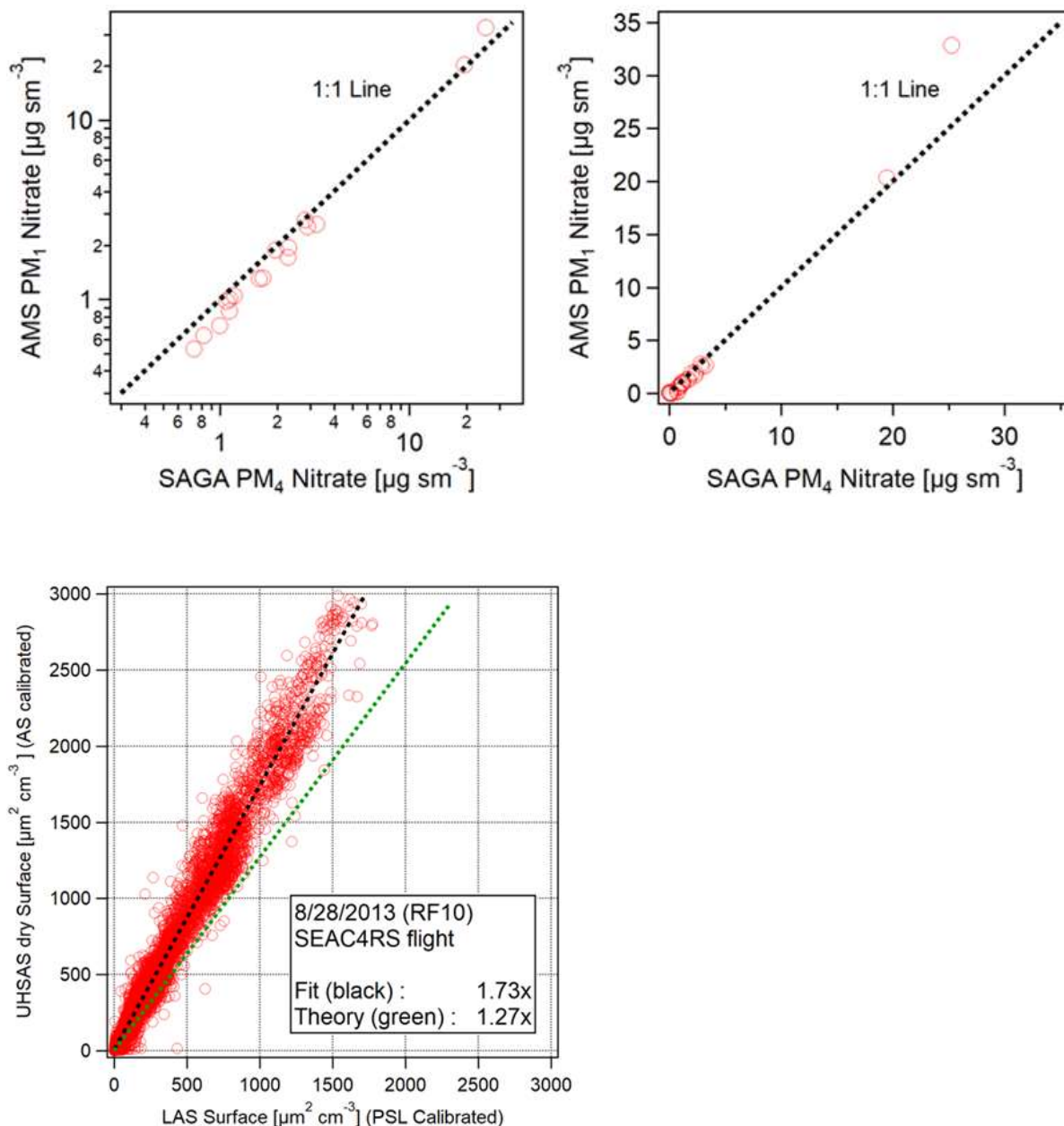
Figure S8. (top) Comparison of particulate nitrate observed by the AMS and SAGA instruments. The AMS has a size cut of ~1 micron, while SAGA samples up to 4 microns. AMS data are averaged over the SAGA sampling interval (~5 minutes) for all Rim Fire observations. Data is shown on both a log (left) and linear (right) scale. (bottom) Comparison of aerosol surface area observed by the LAS and UHSAS instruments. Low bias in the LAS results from the use of PSLs for size calibration instead of ammonium sulfate (P. Campuzano-Jost, personal communication, 2021).
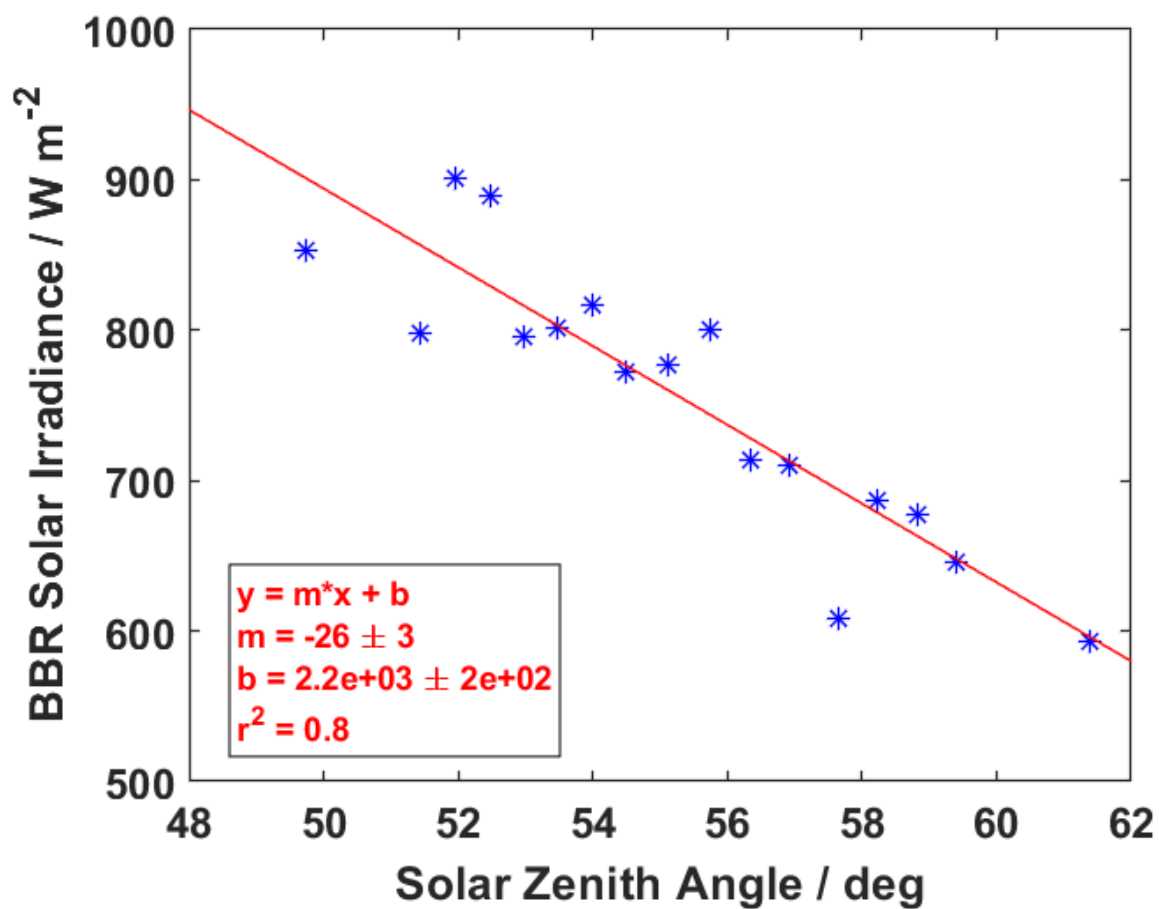
Figure S9. Linear relationship between solar zenith angle and total (up + down) solar irradiance from the broadband radiometer (BBR) instrument. The red line represents an ordinary least-squares fit, used to estimate irradiance for the parameterization of $NO_2$ reactive uptake.
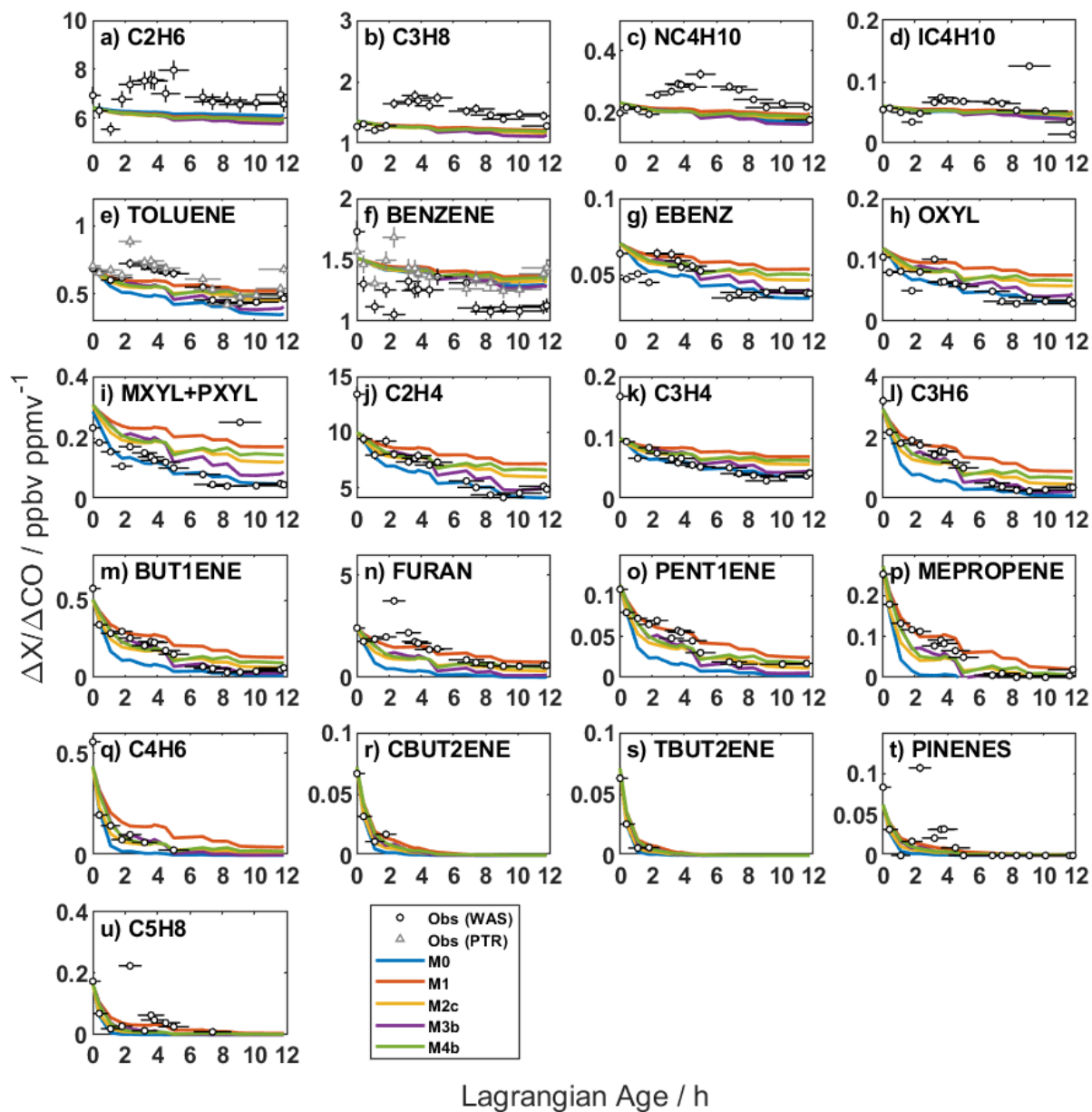
Figure S10. Age evolution of NEMRs for all observed VOC. Black circles and gray triangles are observations from the WAS and PTR-MS, respectively, with their corresponding uncertainty due to measurement accuracy and age. Species, in order from a) to u), are: ethane, propane, n-butane, i-butane, toluene, benzene, ethyl benzene, o-xylene, m-xylene + p-xylene, ethene, propadiene, propene, 1-butene, furan, 1-pentene, methyl propene (isobutene), 1,3-butadiene, cis-2-butene, trans-2-butene, $\alpha$-pinene + $\beta$-pinene, and isoprene. Colored lines are model output from the base simulation (M0, blue), addition of unmeasured VOC (M1, red), and addition of unmeasured VOC and primary HONO (M2c, yellow), secondary HONO via $pNO_3^-$ photolysis (M3b, purple), or $NO_2$ heterogeneous uptake (M4b, green). Note that the furan observation is the difference between PTR-MS (furan + isoprene) and WAS isoprene.
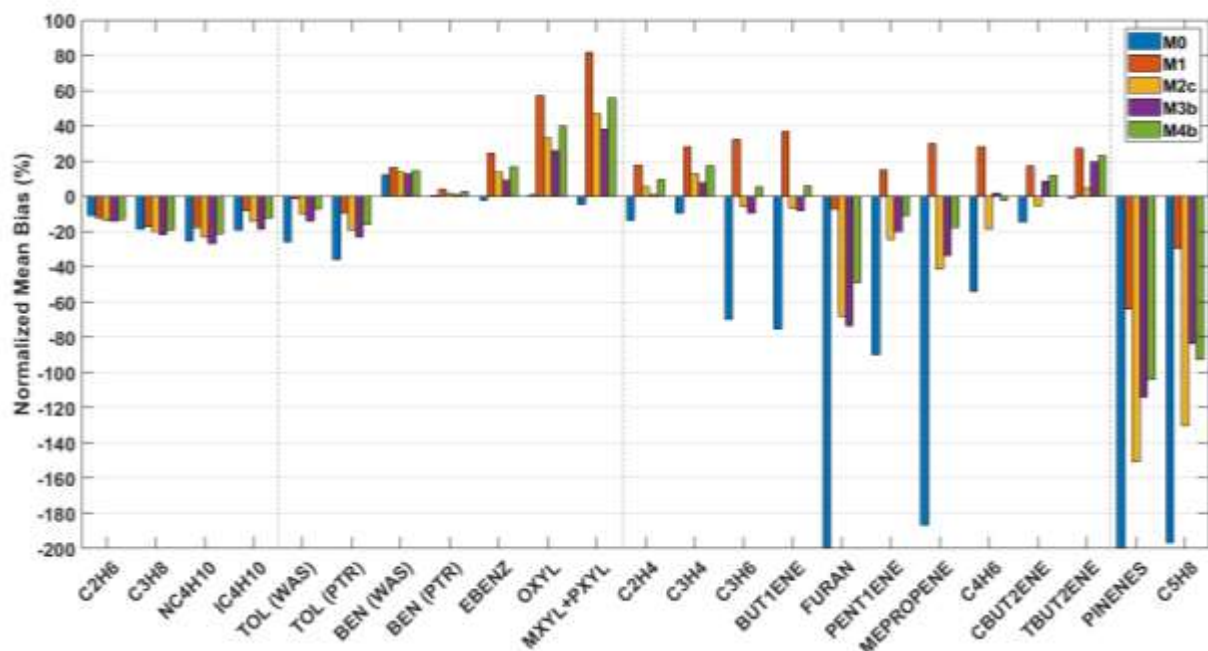
Figure S11. Normalized mean bias (NMB) of modeled VOC profiles compared to observations. For each simulation and each VOC, NMB is computed with model output shown in the previous figure following Gustafson and Yu (2012). Negative bias means that the model is lower than observations on average. Vertical dotted lines demarcate the four groups discussed in the main text.
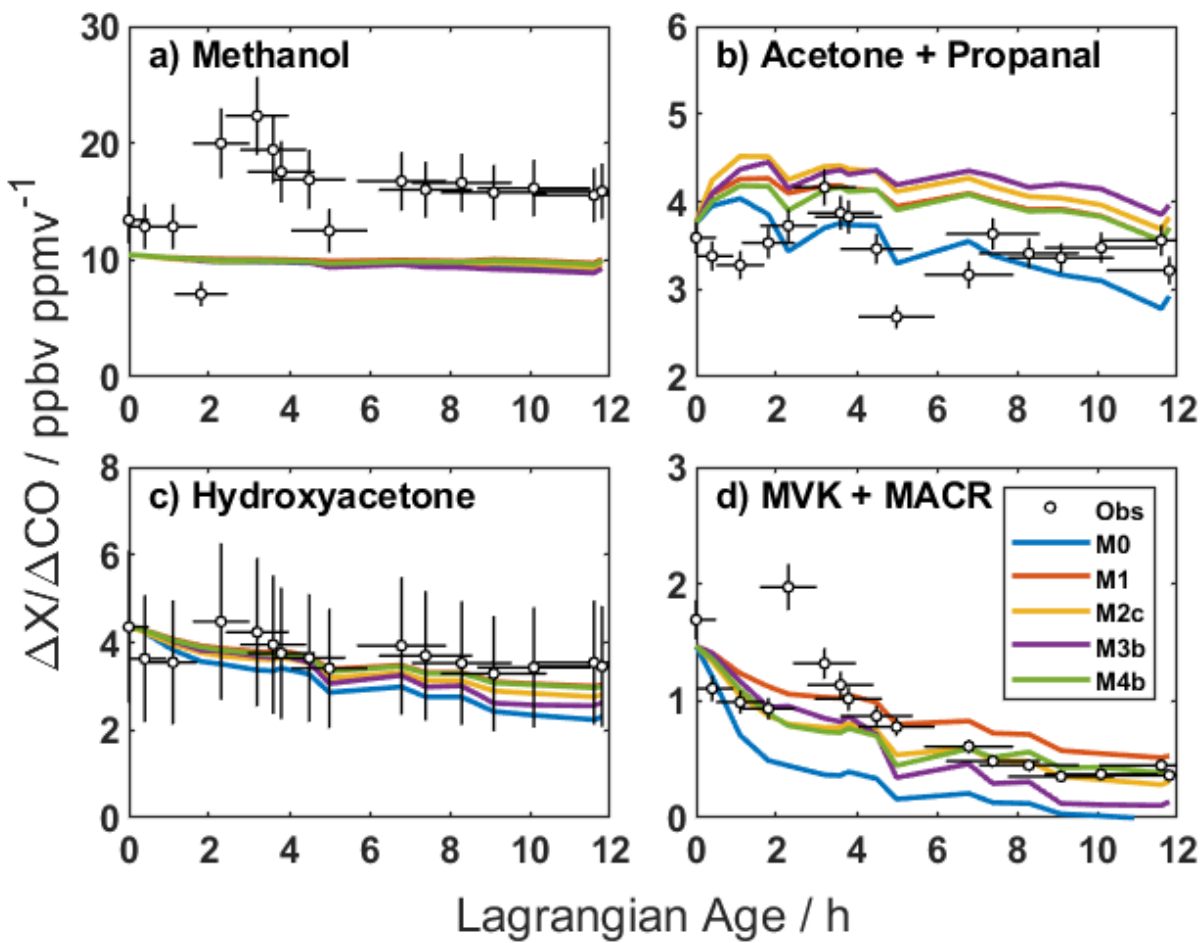
Figure S12. Age evolution of NEMRs for oxygenated VOC. Black circles are observations with their corresponding uncertainty due to measurement accuracy and age. Colored lines are as described in Fig. S10.
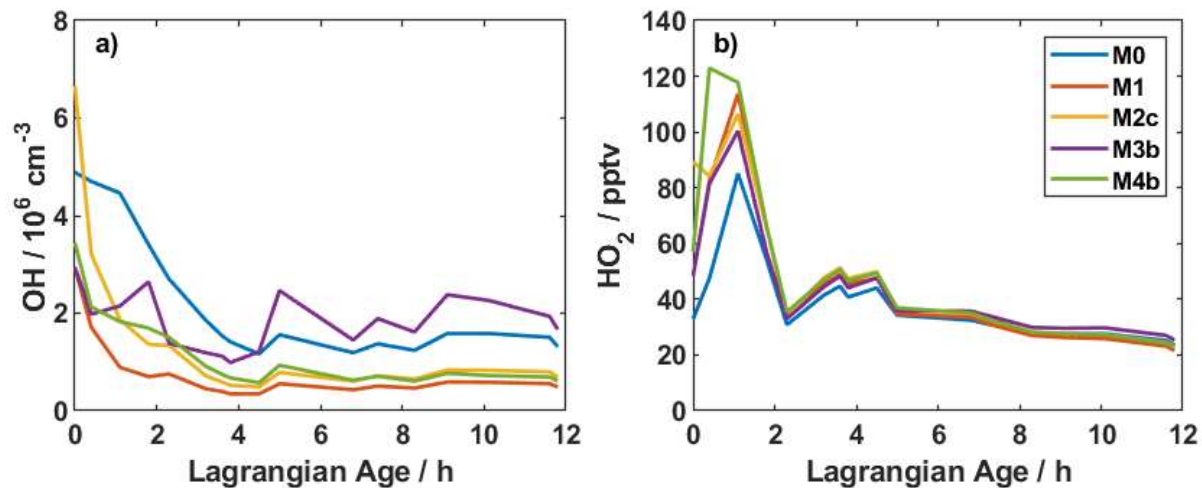
Figure S13. Age evolution of model-predicted OH concentration (a) and $HO_2$ mixing ratio (b). Colors are as described in Fig. S10.
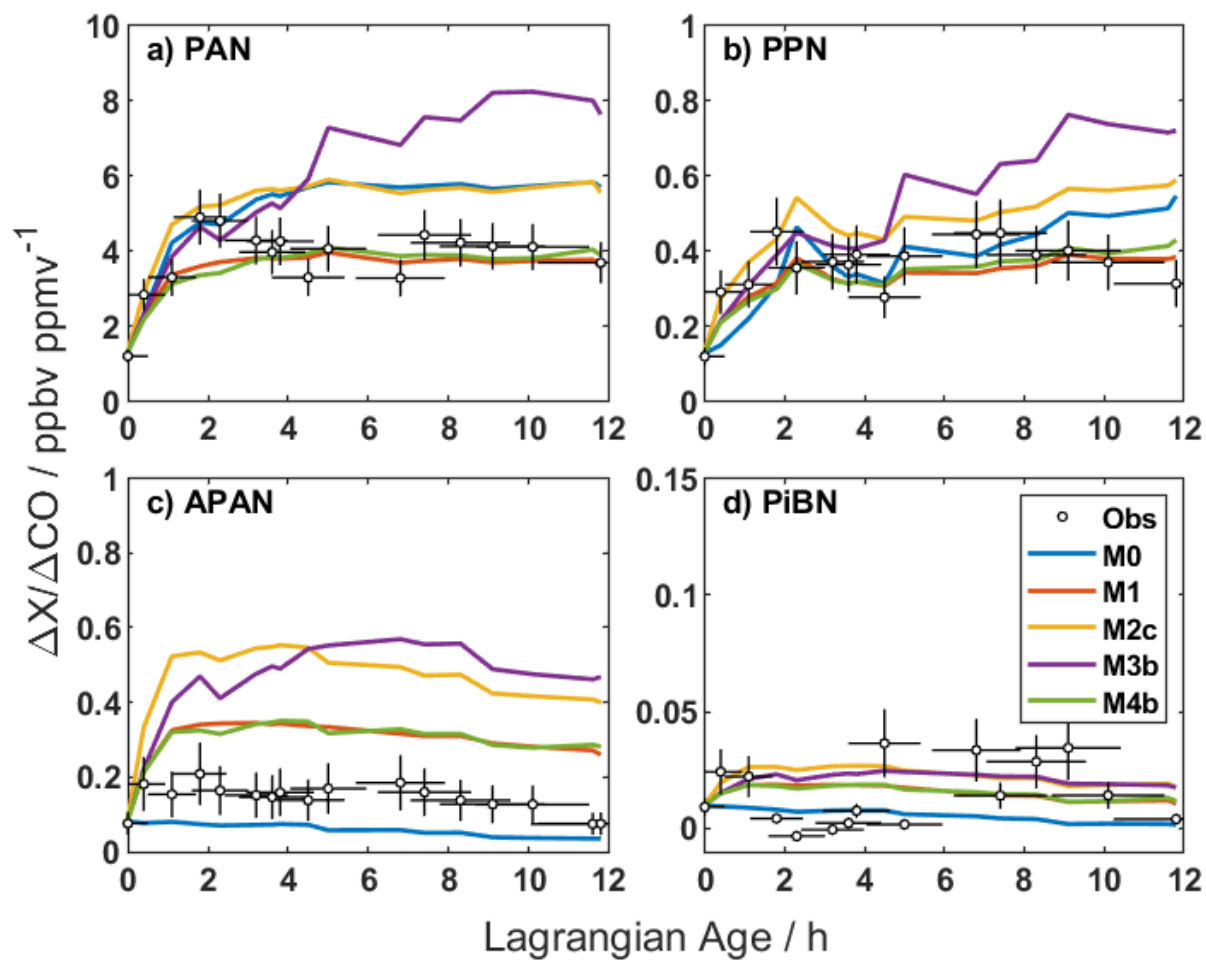
Figure S14. Age evolution of NEMRs for speciated peroxynitrates. Black circles are observations with their corresponding uncertainty due to measurement accuracy and age. Colored lines are as described in Fig. S10.
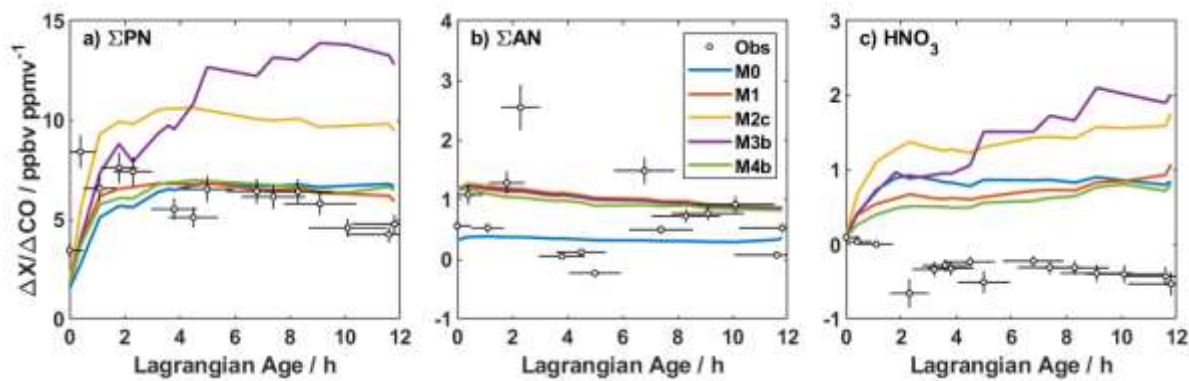
Figure S15. Age evolution of NEMRs for total peroxy nitrates (a), total alkyl nitrates (b), and nitric acid (c). Black circles are observations with their corresponding uncertainty due to measurement accuracy and age. Colored lines are as describe in Fig. S10. MCM PN and AN species are identified using simplified molecular-input line-entry system (SMILES) strings and SMILES filtering code provided with F0AM. Model $HNO_3$ NEMRs deviate significantly from observations because the model does not account for gas-to-particle nitrate partitioning.
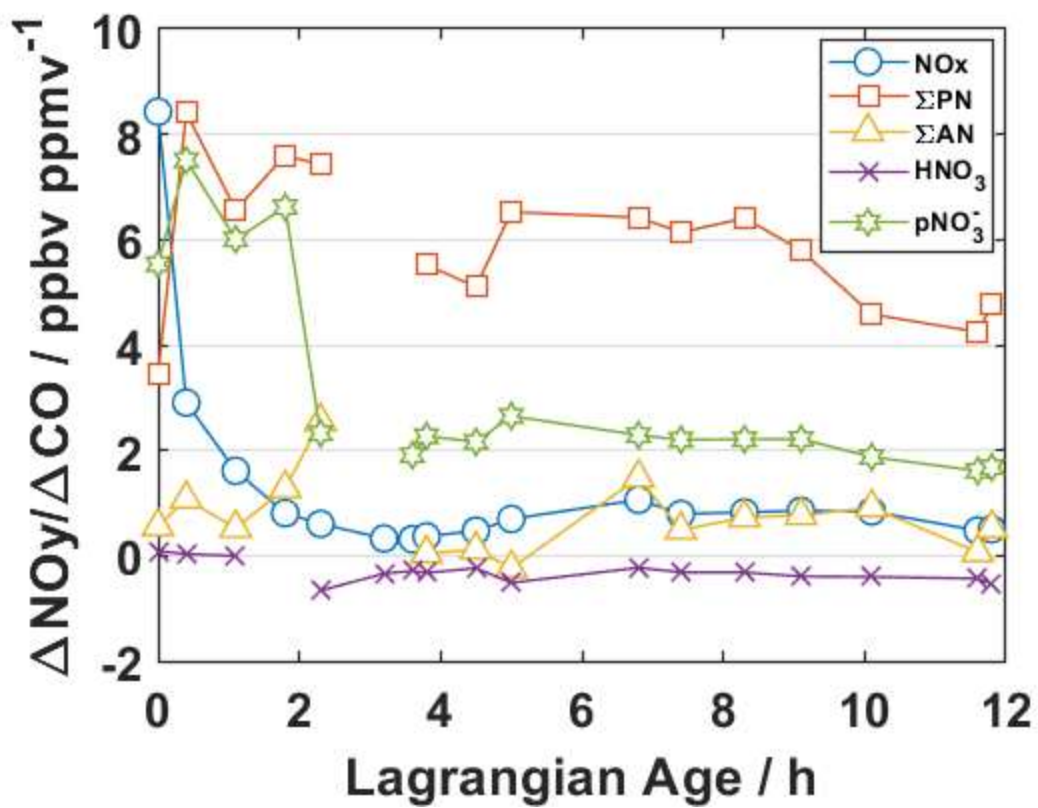
Figure S16. Comparison of age trends for different components of observed $NO_y$, including $NO_x$ (blue circles), total peroxy nitrates (red squares), total alkyl nitrates (yellow triangles), nitric acid (purple X), and particulate nitrate (green stars).
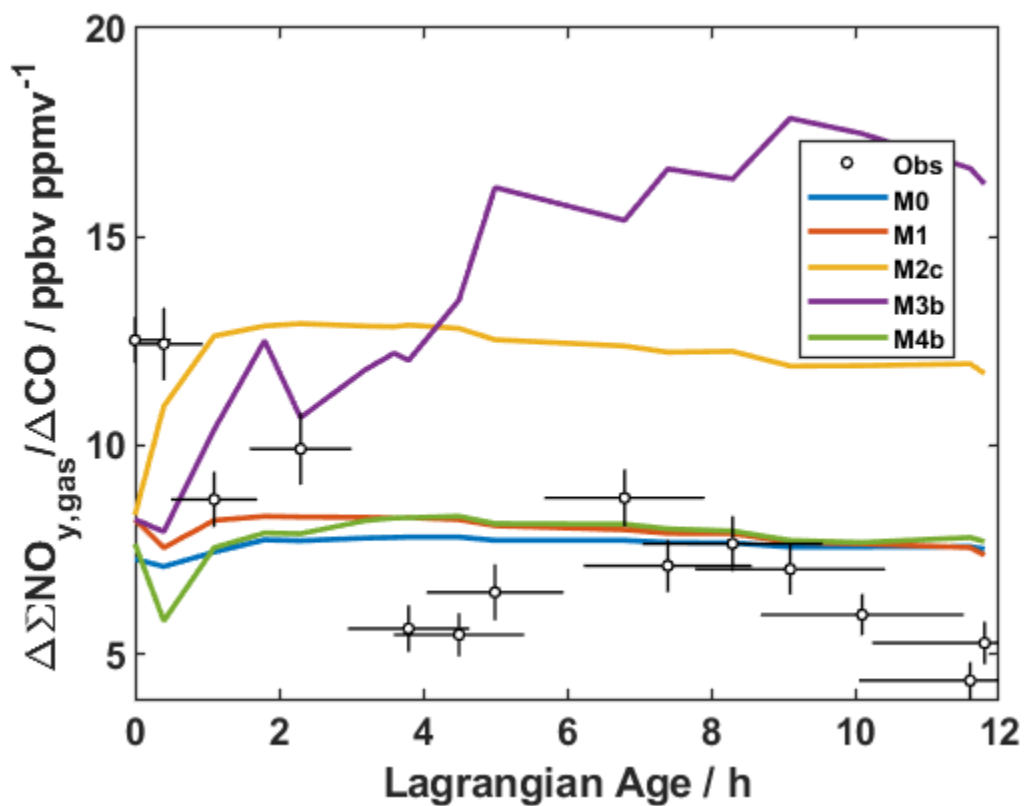
Figure S17. Age evolution of modelled gas-phase $NO_y$. Symbols and lines are as described Fig. S10. Observed values represent the sum of $NO_x$, $\Sigma PN$, $\Sigma HN$, and $HNO_3$. Model values represent the sum over the same modelled species and thus exclude HONO, $HO_2NO_2$, and nitroaromatics.
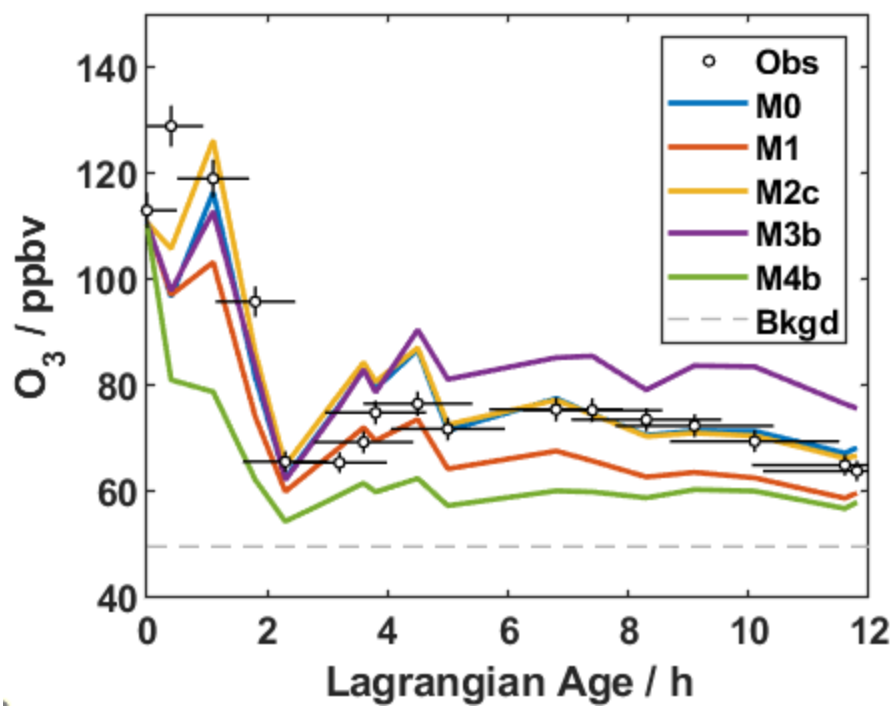
Figure S18. Age evolution of absolute ozone mixing ratio. Symbols and lines are as described Fig. S10. The grey dashed line denotes the estimated $O_3$ background mixing ratio.
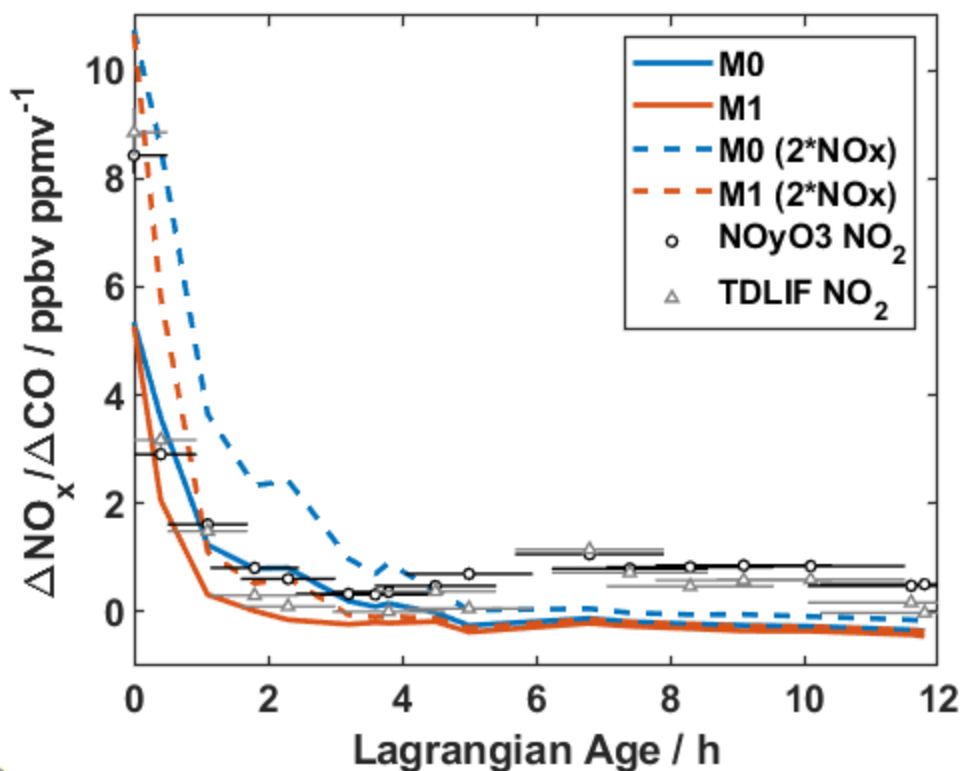
Figure S19. Comparison of $NO_x$ NEMRS for observations (symbols), simulations M0/M1 (solid lines), and sensitivity perturbations where initial $NO_x$ is doubled (dashed lines). For observations, black circles and gray triangles represent $NO_x$ calculated with two different $NO_2$ measurements and the same NO measurement (from the NOyO3 instrument). Error bars denote uncertainty due to age estimation. Uncertainty due to measurement accuracy is small (4%).
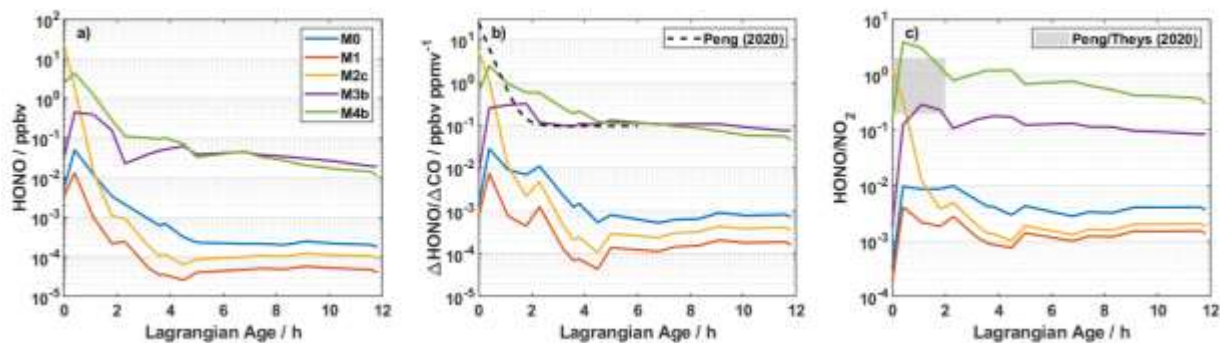
Figure S20. Age evolution of simulated absolute HONO mixing ratios (a), HONO NEMRs (b), and the ratio of HONO to $NO_2$ (c). Colored lines are as described in Fig. S10. In (b), the black dashed line shows the fitted line from Fig. 3 of Peng et al. (2020). In (c), the shaded gray area is the range of values reported by Peng et al. (2020) and Theys et al. (2020).
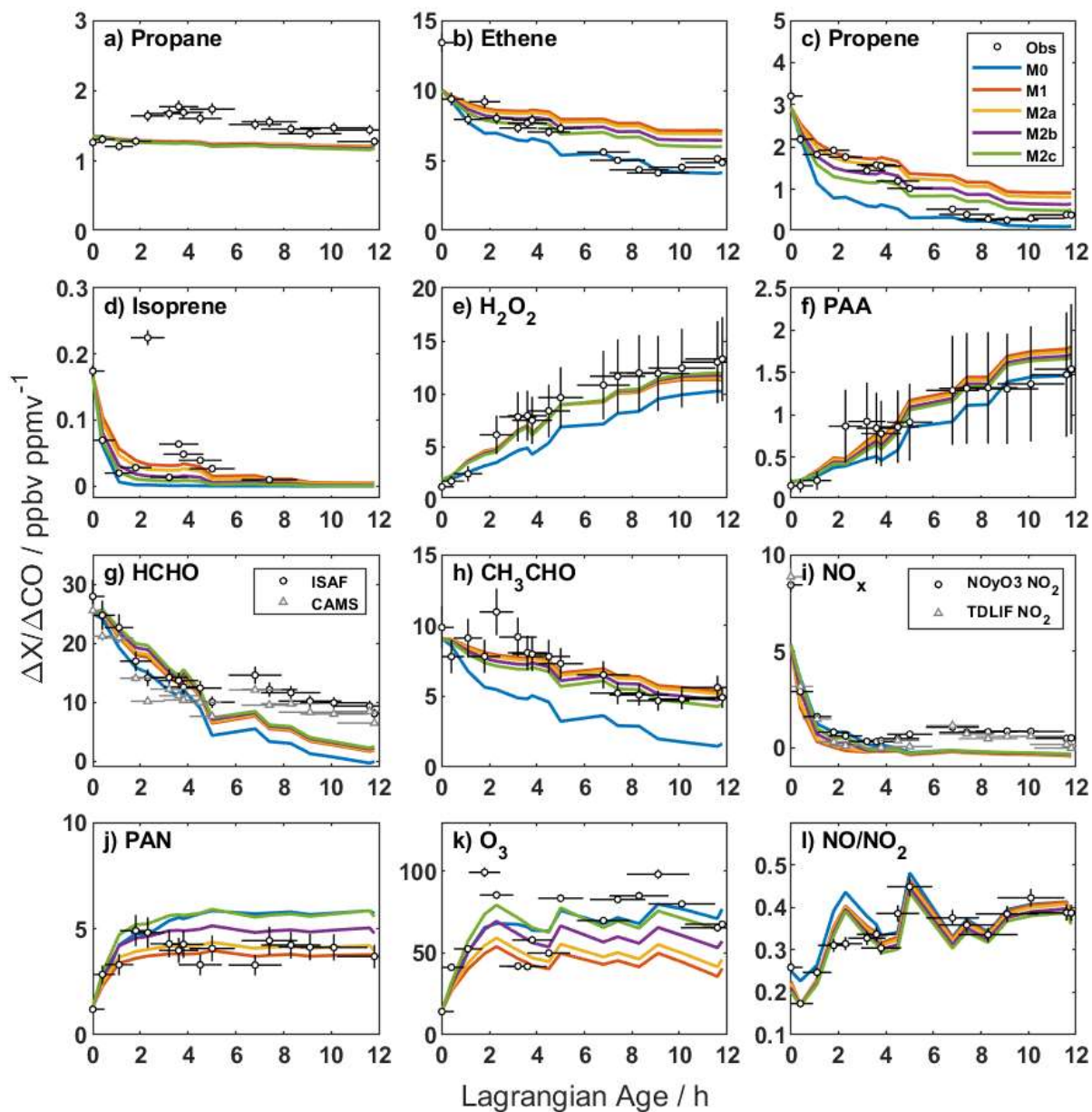
Figure S21. Age evolution of NEMRs for sensitivity simulations to assumed initial HONO concentration. Black circles are observations with their corresponding uncertainty due to measurement accuracy and age. Colored lines are model output from the base simulation (M0, blue), addition of unmeasured VOC (M1, red), and addition of unmeasured VOC plus primary HONO at mixing ratios of 5, 15, and 25 ppbv (yellow, purple, and green, respectively).
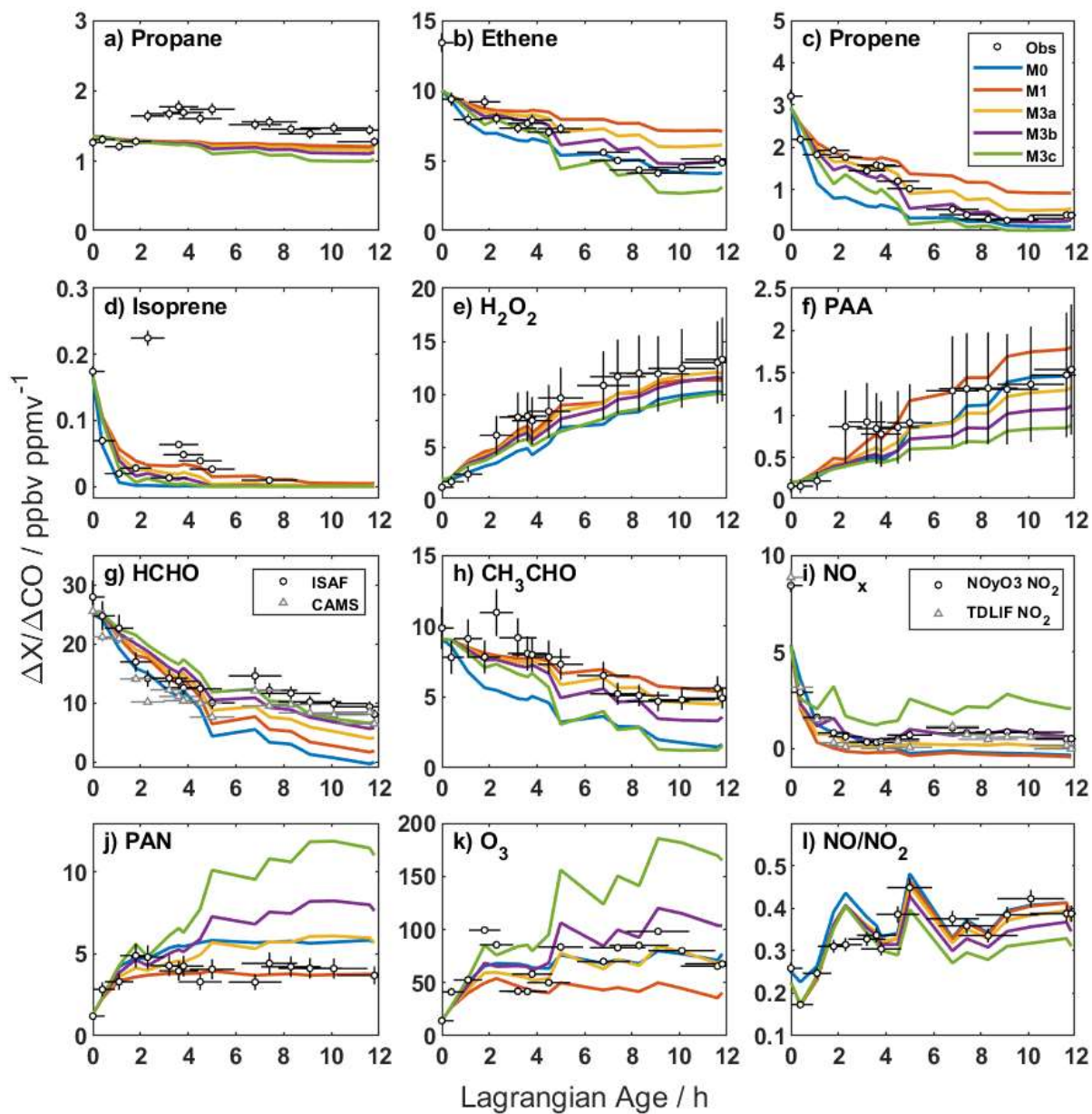
Figure S22. Age evolution of NEMRs for sensitivity simulations to particulate nitrate photolysis. Black circles are observations with their corresponding uncertainty due to measurement accuracy and age. Colored lines are model output from the base simulation (M0, blue), addition of unmeasured VOC (M1, red), and addition of unmeasured VOC plus $pNO_3^-$ photolysis with rate multipliers of 0.5, 1, and 2 (yellow, purple, and green, respectively).
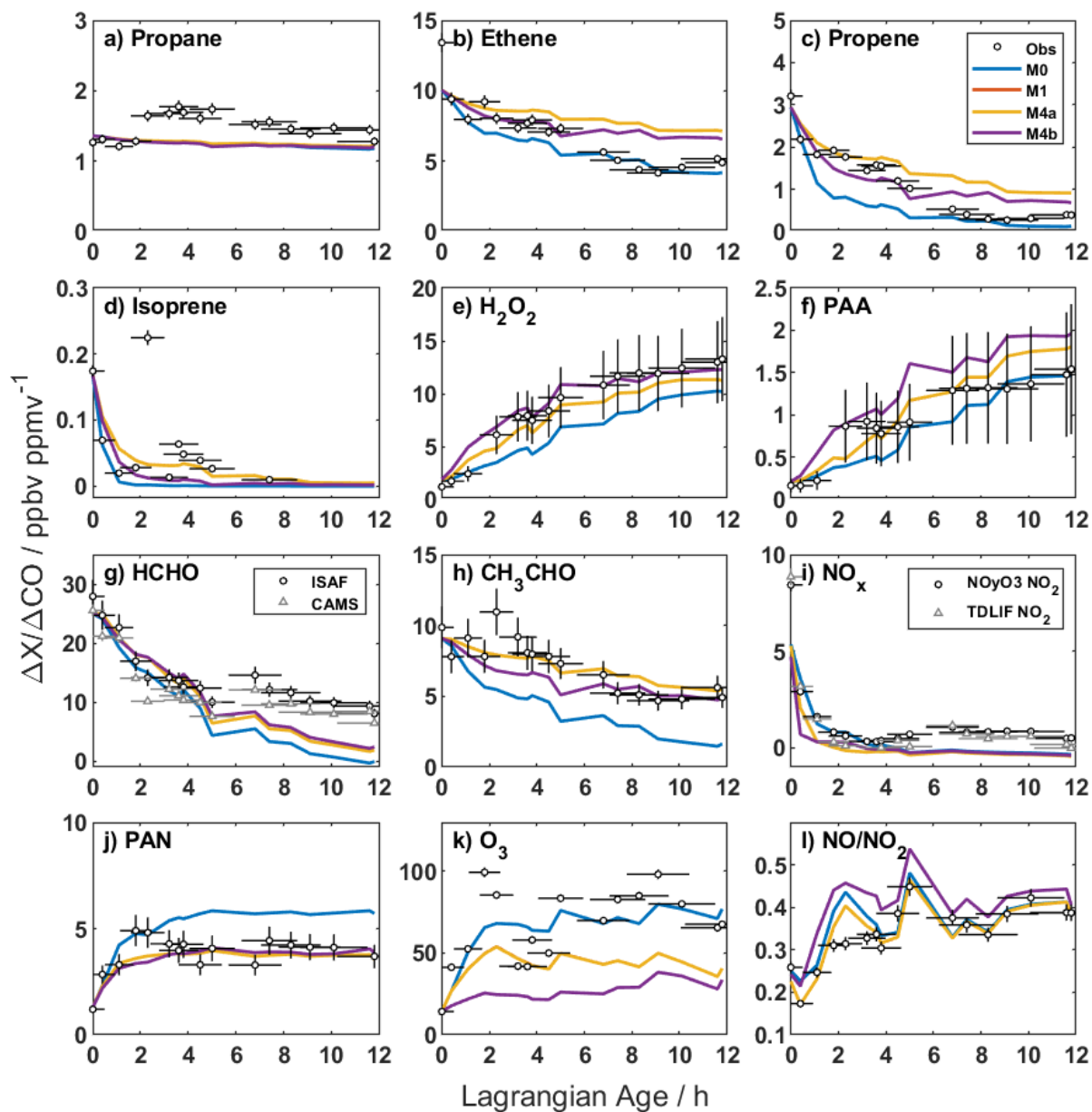
Figure S23. Age evolution of NEMRs for sensitivity simulations to heterogeneous reaction of NO$_2$. Black circles are observations with their corresponding uncertainty due to measurement accuracy and age. Colored lines are model output from the base simulation (M0, blue), addition of unmeasured VOC (M1, red), and addition of unmeasured VOC plus NO2 heterogeneous reaction with rate multipliers of 1 and 1000 (yellow and purple, respectively). Note that there is no visible difference in model output for simulations M1 and M4a.
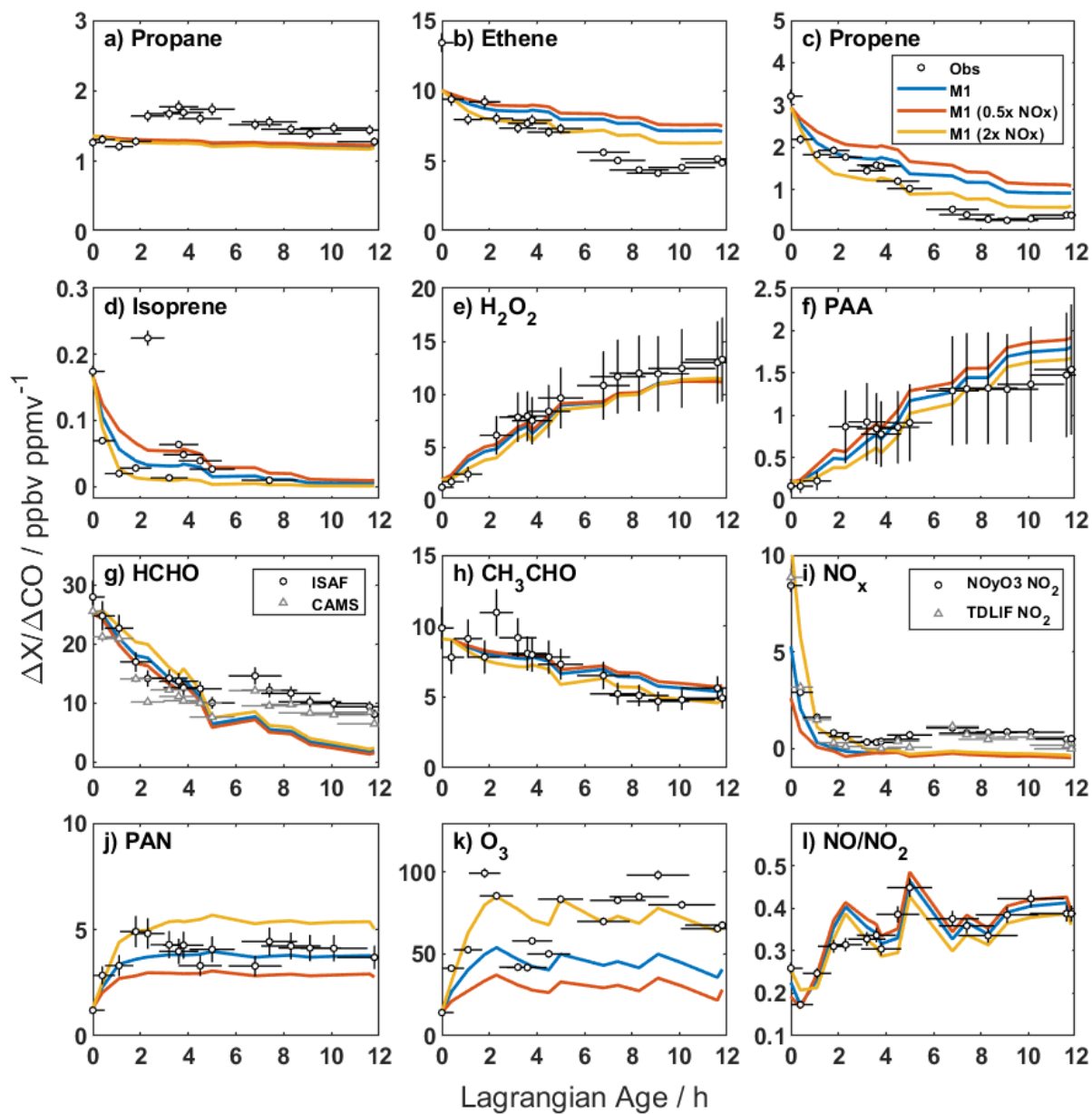
Figure S24. Age evolution of NEMRs for sensitivity simulations to initial $NO_x$. Simulation M1 (blue line) is modified by multiplying initial NO and $NO_2$ mixing ratios by a factor of 0.5 (red) or 2 (yellow). Other details are as described in Fig. 2 of the main text.
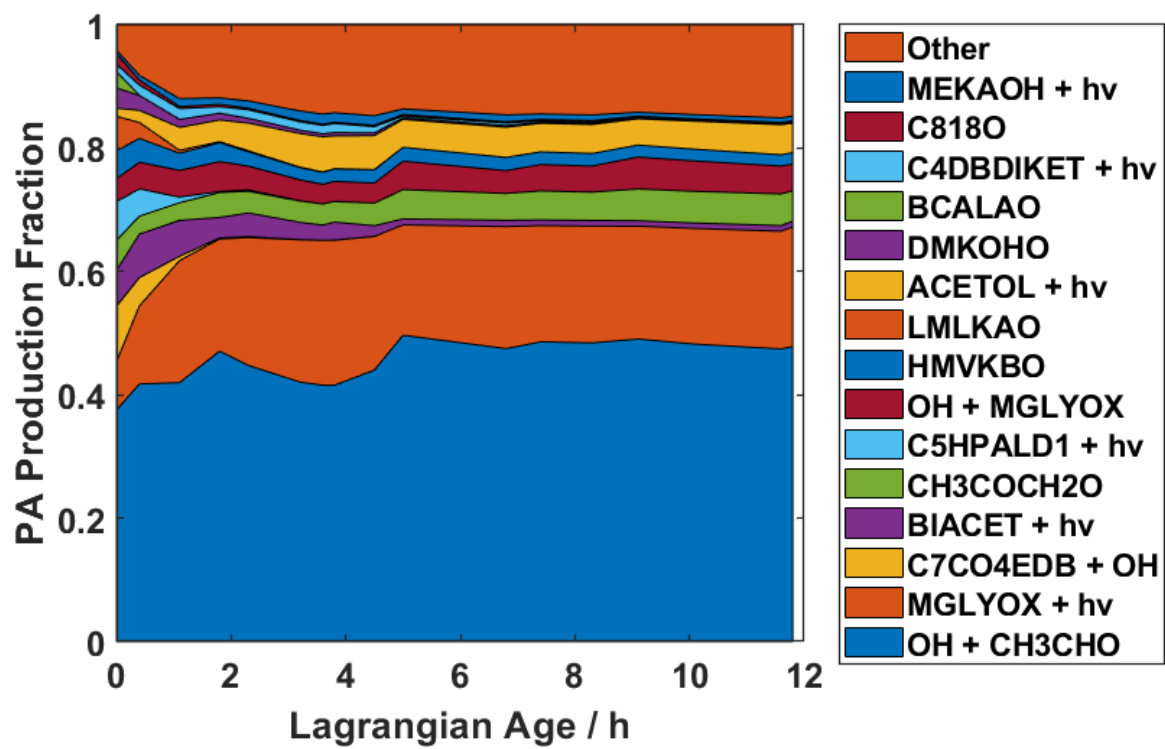
Figure S25. Fractional contributions to production of peroxyacetyl radical in simulation M3b.
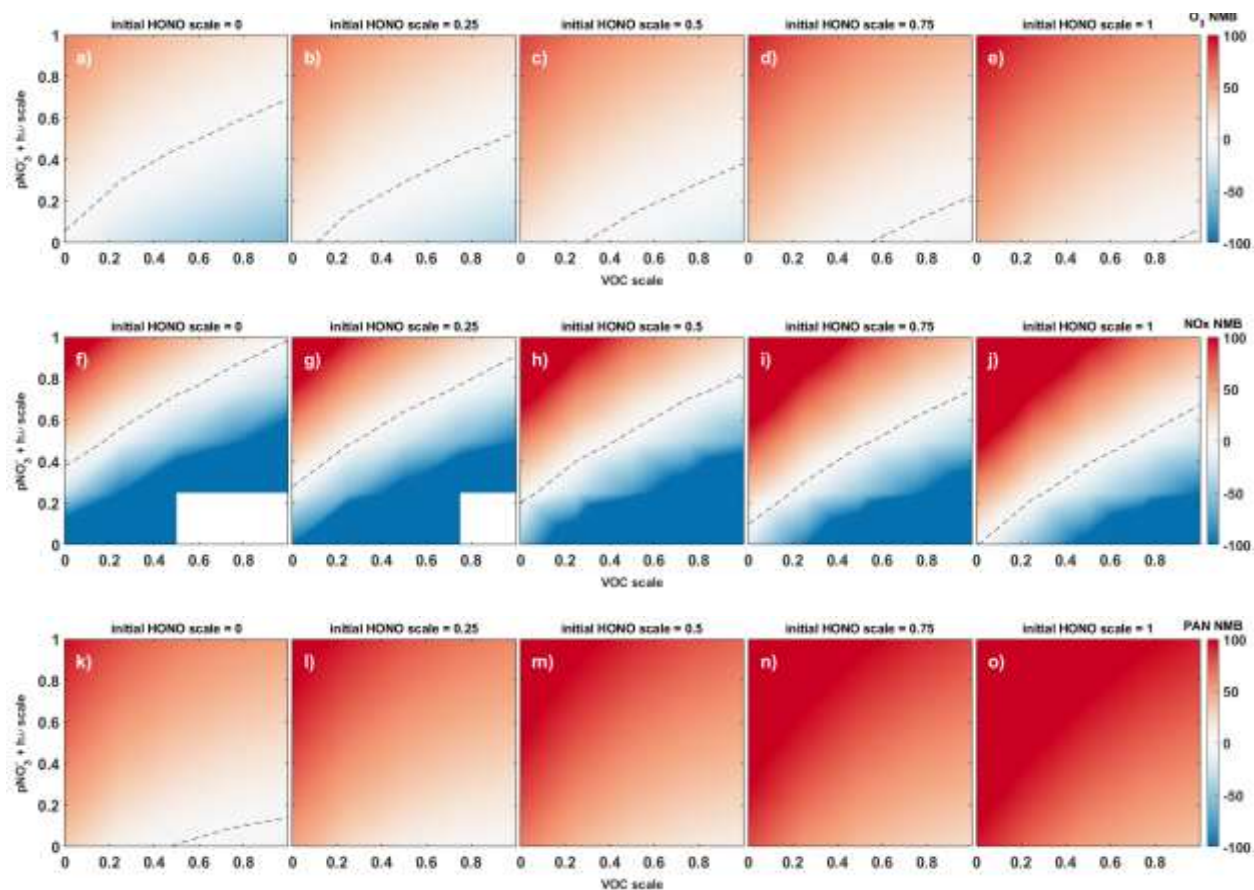
Figure S26. NMB of NEMRs for ozone (a-e), NOx (f-j), and PAN (k-o) for the sensitivity simulations described in SI Text S4. Simulations involve iteratively scaling unmeasured VOC (x-axis), $pNO_3^-$ photolysis (y-axis), and initial HONO (columns) by factors of 0, 0.25, 0.5, 0.75, and 1. Shading indicates NMB of simulation NEMRs against observations, ranging from negative (blue) to positive (red) values. Dashed lines indicate interpolated contours for NMB of zero, corresponding to values shown in Fig. S27.
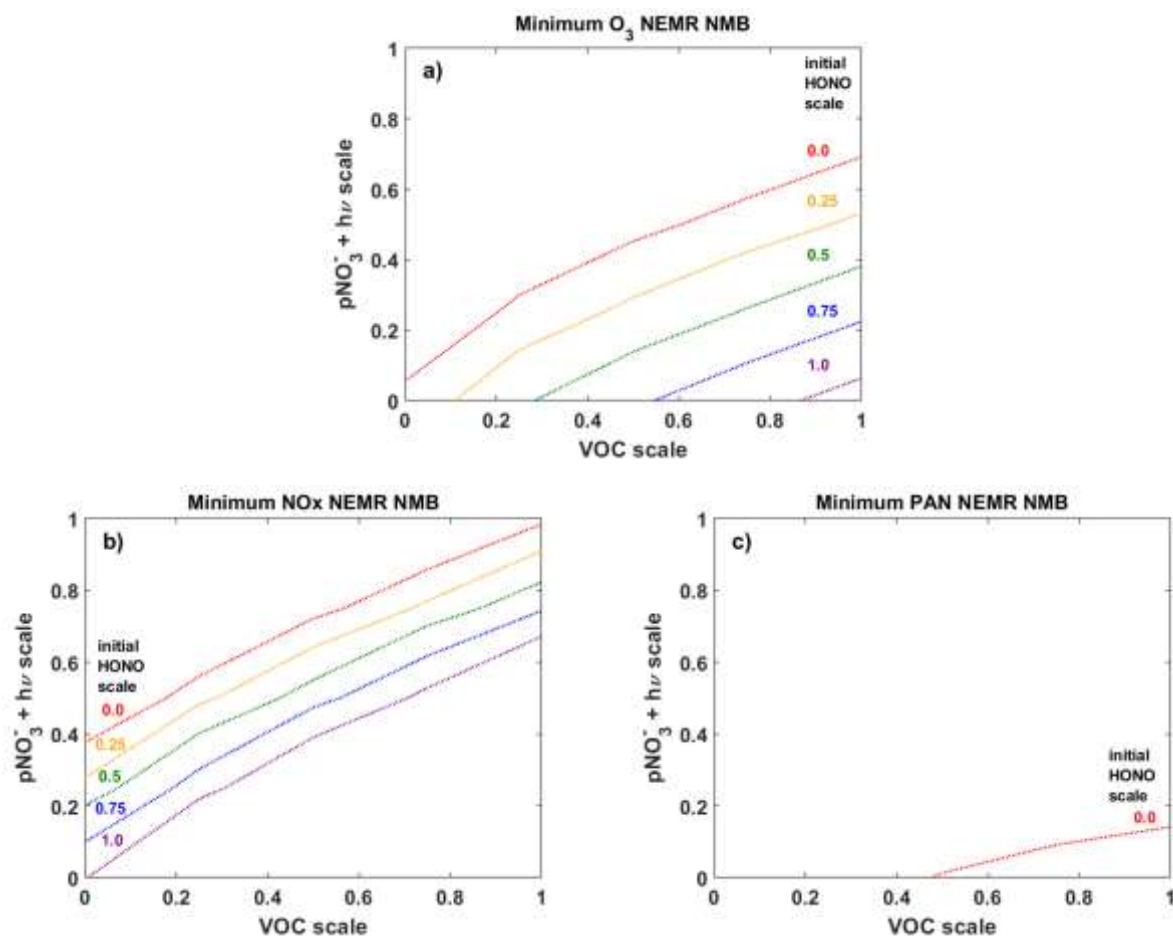
Figure S27. Isopleths for net-zero values of the normalized mean bias (NMB) for NEMRs of ozone (a), $NO_x$ (b), and PAN (c). Each colored dotted line represents a fixed scaling factor for initial HONO mixing ratios. The x-y coordinates for a point on a given line represent a combination of VOC and $pNO_3^-$ photolysis scaling factors that minimize the $O_3$ NEMR NMB. Isopleths are based on interpolation of results from the optimization simulations (Fig. S26).
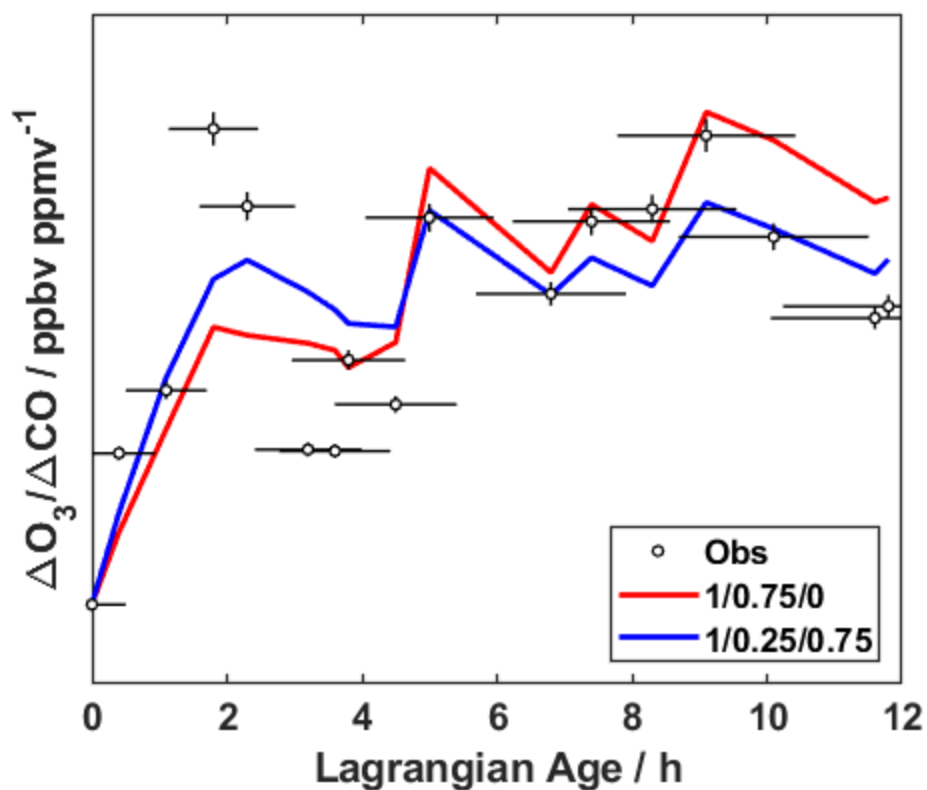
Figure S28. Comparison of observed $O_3$ NEMRs with those from two optimization simulations (SI Text S4) with near-zero ozone NMB (red: VOC scale = 1, $pNO_3^-$ + hν scale = 0.75, initial HONO scale = 0; purple: VOC scale = 1, $pNO_3^-$ + hν scale = 0.25, initial HONO scale = 0.75).